J Physiol 590.18 (2012) pp 4403–4422

The Journal of Physiology

Modelling cardiac calcium sparks in a three-dimensional reconstruction of a calcium release unit

Johan Hake[1,2], Andrew G. Edwards[1], Zeyun Yu[3], Peter M. Kekenes-Huskey[4], Anushka P. Michailova[1], J. Andrew McCammon[4], Michael J. Holst[5], Masahiko Hoshijima[6,7] and Andrew D. McCulloch[1,6,8]

[1]*Department of Bioengineering, University of California San Diego, CA, USA*
[2]*Simula Research Laboratory, Center for Biomedical Computing, Lysaker, Norway*
[3]*Department of Computer Science, University of Wisconsin-Milwaukee, Milwaukee, WI, USA*
[4]*Howard Hughes Medical Institute, University of California San Diego, CA, USA*
[5]*Department of Mathematics and Physics, University of California San Diego, CA, USA*
[6]*Department of Medicine, University of California San Diego, CA, USA*
[7]*Center for Research in Biological Systems, University of California San Diego, CA, USA*
[8]*Cardiac Biomedical Science and Engineering Center, University of California San Diego, CA, USA*

Key points

- We have developed a detailed computational model of a cardiac Ca^{2+} spark based on a three dimensional reconstruction of electron tomograms.
- Our model predicts near total junctional Ca^{2+} depletion after the spark, while regional Ca^{2+} reserve is preserved. The local Ca^{2+} gradient inferred by these findings reconciles previous model predictions with experimental measurements.
- Differences in local distribution of calsequestrin have a profound impact on spark termination time, as reported by Fluo5, solely based on its Ca^{2+} buffering capacity.
- The SERCA pump can prolong spark release time by pumping Ca^{2+} back into the junctional SR during the spark.

Abstract Triggered release of Ca^{2+} from an individual sarcoplasmic reticulum (SR) Ca^{2+} release unit (CRU) is the fundamental event of cardiac excitation–contraction coupling, and spontaneous release events (sparks) are the major contributor to diastolic Ca^{2+} leak in cardiomyocytes. Previous model studies have predicted that the duration and magnitude of the spark is determined by the local CRU geometry, as well as the localization and density of Ca^{2+} handling proteins. We have created a detailed computational model of a CRU, and developed novel tools to generate the computational geometry from electron tomographic images. Ca^{2+} diffusion was modelled within the SR and the cytosol to examine the effects of localization and density of the Na^+/Ca^{2+} exchanger, sarco/endoplasmic reticulum Ca^{2+}-ATPase 2 (SERCA), and calsequestrin on spark dynamics. We reconcile previous model predictions of approximately 90% local Ca^{2+} depletion in junctional SR, with experimental reports of about 40%. This analysis supports the hypothesis that dye kinetics and optical averaging effects can have a significant impact on measures of spark dynamics. Our model also predicts that distributing calsequestrin within non-junctional Z-disc SR compartments, in addition to the junctional compartment, prolongs spark release time as reported by Fluo5. By pumping Ca^{2+} back into the SR during a release, SERCA is able to prolong a Ca^{2+} spark, and this may contribute to SERCA-dependent changes in Ca^{2+} wave speed. Finally, we show that including the Na^+/Ca^{2+} exchanger inside the dyadic cleft does not alter local $[Ca^{2+}]$ during a spark.

(Received 29 January 2012; accepted after revision 10 April 2012; first published online 10 April 2012)

Corresponding author J. E. Hake: Simula Research Laboratory, Scientific Computing, PO Box 134, Lysaker, Norway. Email: johan.hake@gmail.com

Abbreviations CICR, Ca^{2+} induced Ca^{2+} release; CRU, Ca^{2+} release unit; CMDN, calmodulin; CSQN, calsequestrin; EC, excitation–contraction; jSR, junctional sarcoplasmic reticulum; NCX, Na^+/Ca^{2+} exchanger; ODE, ordinary differential equation; PDE, partial differential equation; RyR, ryanodine receptor; SERCA, sarco/endoplasmic reticulum Ca^{2+}-ATPase 2; SR, sarcoplasmic reticulum; TRPN, troponin C.

DOI: 10.1113/jphysiol.2012.227926

Introduction

Cardiac excitation–contraction (EC) coupling is a multi-scale phenomenon. In a ventricular cardiomyocyte, Ca^{2+}-induced Ca^{2+} release (CICR) is initiated by opening of L-type Ca^{2+} channels. This permits influx of Ca^{2+}, which rapidly diffuses across the dyadic cleft to activate local ryanodine receptors (RyRs), and cause sarcoplasmic reticulum (SR) Ca^{2+} release. This cleft, along with the local SR structures, and t-tubular membrane with its ensemble of L-type channels, forms the fundamental structural unit of EC coupling – the Ca^{2+} release unit (CRU) (Stern, 1992). The elementary event of EC coupling is activation of a single CRU (a Ca^{2+} spark), and synchronous activation of the 10,000 CRUs in an average ventricular myocyte results in fusion of these unitary events into the whole-cell Ca^{2+} transient (Cheng *et al.* 1993). While the dynamics of single spontaneous sparks, as we study here, are subtly different from those occurring during triggered CICR, the fundamental governing processes are likely to be very similar (Picht *et al.* 2011).

Ensemble effects involving the recruitment of CRUs play an important role in several key features of normal EC coupling, notably graded release and voltage-dependent gain (Rice *et al.* 1999; Altamirano & Bers, 2007), but also in abnormal behaviour associated with pathological coupling (Restrepo *et al.* 2008; Cooper *et al.* 2010; Swietach *et al.* 2010). At the level of the CRU, the kinetics of L-type channel and RyR gating are clearly important, as are the limits imposed by cytosolic Ca^{2+} diffusion, which is sensitive to the local structural geometry (Stern, 1992; Hinch *et al.* 2004). However, a number of additional characteristics, such as protein localization in the SR and t-tubular membranes, and intra-SR Ca^{2+} diffusion, are thought to be of importance to CRU function but are not well understood (Picht *et al.* 2011; Sobie & Lederer, 2012).

Given the constraints imposed by optical diffraction, and the temporal and equilibrium characteristics of available Ca^{2+} fluorophores (Sobie & Lederer, 2012), quantitative computational approaches have proven to be useful for the study of local CRU dynamics (Sobie *et al.* 2002; Louch *et al.* 2010; Ramay *et al.* 2010; Picht *et al.* 2011). However, to date, models have employed simplified schematic representations of the individual release unit, which lack the geometric complexities of the relevant subcellular structures, particularly the local SR compartments. In the current study we have attempted to model spark dynamics in a three-dimensional reconstruction of a single release unit of a mouse ventricular myocyte. The local compartment geometries were defined by electron tomography images, which were manually segmented and reconstructed to form a finite element mesh suitable for solution of reaction-diffusion problems (Yu *et al.* 2008*a*; Hayashi *et al.* 2009).

With this model, we examined questions related to the roles of Ca^{2+} dye kinetics within SR, and localization of Ca^{2+} handling proteins in the CRU and CRU-associated membrane structures in determining spark characteristics. We report several novel conclusions. (i) Temporal characteristics of the low affinity Ca^{2+} dye, Fluo5, combined with diluting effects of a relatively large optical recording volume (compared to a single junctional SR terminal), cause experimental records of F/F_0 to under-report local junctional SR (jSR) Ca^{2+} depletion during a Ca^{2+} blink. This finding reconciles previous model predictions of high local Ca^{2+} depletion in the jSR of 90% (Sobie *et al.* 2002) with the less severe depletion reported experimentally of 40% (Zima *et al.* 2008), and supports the hypothesis that dye kinetics and optical averaging effects have a substantial impact on measures of spark dynamics (Sobie & Lederer, 2012). Our analyses suggest that, at the time of spark termination, the true local jSR Ca^{2+} depletion is much closer to 90% than 40%. (ii) Distributing calsequestrin (CSQN) within non-junctional Z-disc SR compartments as suggested by immuno-staining studies (Jorgensen *et al.* 1985, 1993; Scriven *et al.* 2000), in addition to the junctional compartment, prolongs spark release time and decreases the mean amplitude of release flux. (iii) Sarco/endoplasmic reticulum Ca^{2+}-ATPase (SERCA) functioning at the non-junctional face of the jSR within the CRU domain are capable of prolonging release time. This mechanism may help to explain the experimentally observed reduction of Ca^{2+} wave velocity when SERCA is inhibited (Keller *et al.* 2007). (iv) Including the Na^+/Ca^{2+} exchanger (NCX) within the dyad, the validity of which has been debated (Trafford *et al.* 1995; Scriven *et al.* 2000; Jayasinghe *et al.* 2009), does not substantially alter the total release flux during a spontaneously activated Ca^{2+} spark.

Methods

Geometry

A highly detailed computational geometry of a CRU was generated from electron tomograms of a mouse ventricular myocyte (Hayashi *et al.* 2009). Features were first manually segmented from the images using the open source and cross platform software tool IMOD (Kremer *et al.* 1996); see Fig. 1*A*. See the online Supplemental Material for a movie of the segmented features. The initial surface mesh, generated from the segmented features, had many small and sharp triangles and hence was of poor quality for numerical analysis. The surface

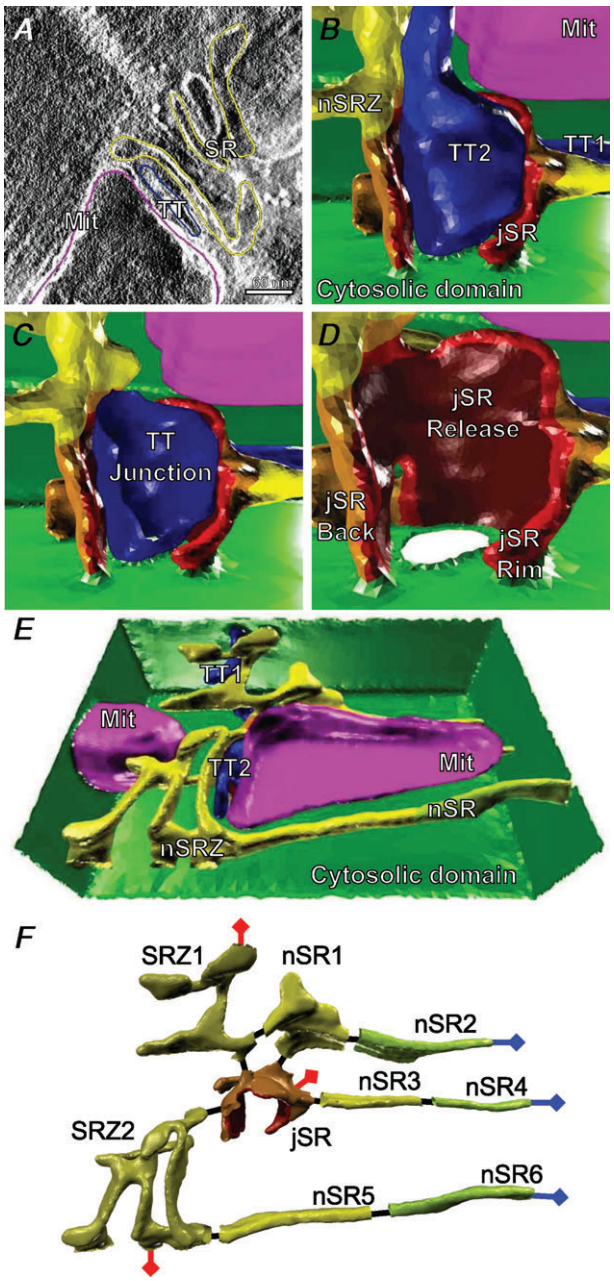

Figure 1. Geometry generation
A, the Ca^{2+} release unit (CRU) was manually segmented from a stack of electron tomography images. Here parts of a single tomogram are shown. The segmented features are: mitochondria (pink), sarcoplasmic reticulum (SR) (yellow) and t-tubules (blue). *B*, the CRU is formed by junctional SR (jSR) wrapping around the t-tubule. The t-tubule boundary in the CRU is split into two distinct boundaries, junctional and non-junctional. In *C*, the junctional part is shown. The boundary of jSR is split into three distinct boundaries. jSR Back (orange), jSR Release (dark red) and jSR Rim (red). *D*, the junctional part with the t-tubule completely removed. Here one clearly sees the Release boundary. *E*, the segmented geometry is eventually turned into a high quality annotated surface mesh. Here for visualization purposes it is shown with the upper and front side removed. The dimension of the mesh is: 1430 × 940 × 406 nm. *F*, the SR is divided into nine distinct compartments, 1 jSR, 2 Z-line SR compartments, and 6 network SR compartments. Each SR compartment interfaces with the cytosol across the boundaries shown here. The compartments are also connected with each other (black lines) and with either the bulk SR compartments (blue lines), or the intermediate SR compartments (red lines), at the limits of the mesh.

mesh was improved using our previously described surface mesh improvement library GAMer (Yu *et al.* 2008*b*; www.fetk.org), installed as a plug-in to Blender (www.blender.org). The improved and annotated mesh can be seen in Fig. 1*B*. See the Supplemental Material for a movie of the annotated surface mesh.

The CRU includes two t-tubules, one longitudinal, TT1, and one transverse, TT2 (Fig. 1*B*). The latter projects through the CRU, and is split into two distinct parts, junctional and non-junctional. In Fig. 1*C* the non-junctional segment is removed to illustrate these two parts: junctional and non-junctional. The jSR boundary is split into three distinct parts: Back (orange), Release (dark red) and Rim (red), see Fig. 1*D*. Ca^{2+} release is applied only to the Release boundary. For some simulations, SERCA flux was applied to the Back boundary. No fluxes were applied to the Rim boundary for any simulation. See below for a thorough description of all fluxes. A tetrahedral mesh, suitable for finite element computation, was then generated within the Blender interface, using TetGen (tetgen.berlios.de), and the marked boundary faces in the surface mesh were similarly marked in the tetrahedral mesh, to apply boundary conditions for the finite element computation. See Supplemental Material for a movie of the annotated tetrahedralized mesh. The final mesh comprised 97,000 vertices and 420,000 tetrahedra.

The physical dimensions of the tetrahedralized mesh are 1430 × 940 × 406 nm with a total volume of the cytosolic domain of 440×10^{-12} μl. The volume of the outer rectangular cuboid was 546×10^{-12} μl, so the volume of the excluded compartments, namely SR, t-tubule and mitochondria, represents 20% of the total volume. The fractional volume of these compartments is larger in a whole cell, ~45% (Page, 1978; Bossen *et al.* 1981), and this discrepancy is likely to be due to the small sample volume of the original image data. The SR was not a component of the volumetric mesh, but included as nine distinct compartments; see Fig. 1*F*. The volume of each SR compartment and the areas and distances between them were measured using tools in Blender and the values are presented in Tables 1 and 2 in the Supplementary Methods section. The average distance between the jSR Release boundary and the junctional t-tubule boundary, i.e. the size of the dyadic cleft, is 15 nm, which is comparable to previous measurements based on EM tomography (Franzini-Armstrong *et al.* 1999; Hayashi *et al.* 2009). The volume of the dyadic cleft

Table 1. Species parameters

Parameter	Description	Value	Ref
D_{Ca}^{cyt}	Diffusion constant of Ca^{2+} in the cytosolic domain	220×10^3 nm^2 ms^{-1}	Louch *et al.* (2010)
D_{Ca}^{sr}	Diffusion constant of Ca^{2+} in the SR compartments	73.3×10^3 nm^2 ms^{-1}¶	
D_{ATP}^{cyt}	Diffusion constant of ATP in cytosol	140×10^3 nm^2 ms^{-1}	Valent *et al.* (2007)
B_{tot}^{ATP}	Total ATP concentration	455 μM*	Bers, (2001)
k_{off}^{ATP}	ATP Ca^{2+} off rate	45 ms^{-1}	Picht *et al.* (2011)
k_{on}^{ATP}	ATP Ca^{2+} on rate	225×10^{-3} ms^{-1} μM^{-1}	Bers, (2001); Picht *et al.* (2011)
K_d^{ATP}	ATP Ca^{2+} dissociation constant	200 μM	Bers, (2001)
D_{CMDN}^{cyt}	Diffusion constant of Calmodulin in cytosol	25×10^3 nm^2 ms^{-1}	Michailova *et al.* (2002)
B_{tot}^{CMDN}	Total calmodulin concentration	24 μM	Fabiato, (1983)
k_{off}^{CMDN}	Calmodulin Ca^{2+} off rate	238×10^{-3} ms^{-1}	Robertson *et al.* (1981)
k_{on}^{CMDN}	Calmodulin Ca^{2+} on rate	34×10^{-3} ms^{-1} μM^{-1}	Robertson *et al.* (1981); Picht *et al.* (2011)
K_d^{CMDN}	Calmodulin Ca^{2+} dissociation constant	7 μM	Picht *et al.* (2011)
B_{tot}^{CSQN}	Total Calsequestrin concentration (only in jSR)	30×10^3 μM†	(Bers, 2001)
B_{tot}^{CSQN}	Total calsequestrin concentration (in all Z-line domain)	6.39×10^3 μM‡	Bers, (2001)
k_{off}^{CSQN}	Calsequestrin Ca^{2+} off rate	65 ms^{-1}	Picht *et al.* (2011)
k_{on}^{CSQN}	Calsequestrin Ca^{2+} on rate	102×10^{-3} ms^{-1} μM^{-1}	Picht *et al.* (2011); Shannon & Bers (1997)
K_d^{CSQN}	Calsequestrin Ca^{2+} dissociation constant	640 μM	Shannon & Bers (1997)
D_{Fluo}^{cyt}	Diffusion constant of Fluo4 in cytosol	42×10^3 nm^2 ms^{-1}	Picht *et al.* (2011)
B_{tot}^{Fluo}	Total Fluo4 concentration	25 μM	Picht *et al.* (2011)
k_{off}^{Fluo}	Fluo4 Ca^{2+} off rate	110×10^{-3} ms^{-1}	Picht *et al.* (2011)
k_{on}^{Fluo}	Fluo4 Ca^{2+} on rate	110×10^{-3} ms^{-1} μM^{-1}	Picht *et al.* (2011)
K_d^{Fluo}	Fluo4 Ca^{2+} dissociation constant	1.1 μM	Picht *et al.* (2011)
D_{Fluo5}^{sr}	Diffusion constant of Fluo5 in SR	8×10^3 nm^2 ms^{-1}	Picht *et al.* (2011)
B_{tot}^{Fluo5}	Total Fluo5 concentration	25 μM	Picht *et al.* (2011)
k_{off}^{Fluo5}	Fluo5 Ca^{2+} off rate	100×10^{-3} ms^{-1}§	
k_{on}^{Fluo5}	Fluo5 Ca^{2+} on rate	250×10^{-6} ms^{-1} μM^{-1}	Picht *et al.* (2011)
K_d^{Fluo5}	Fluo5 Ca^{2+} dissociation constant	400 μM	Picht *et al.* (2011)
$B0_{tot}^{TRPN}$	Total troponin C concentration	70 μM	Bondarenko *et al.* (2004)
d_{tt}	Distance from junctional t-tubule boundary	40 nm	
σ_{tt}	Distance weight	5 nm	
k_{off}^{TRPN}	Troponin C Ca^{2+} off rate	19.6×10^{-3} ms^{-1}	Bondarenko *et al.* (2004)
k_{on}^{TRPN}	Troponin C Ca^{2+} on rate	32.7×10^{-3} ms^{-1} μM^{-1}	Bondarenko *et al.* (2004)
K_d^{TRPN}	Troponin C Ca^{2+} dissociation constant	600×10^{-3} μM	Bondarenko *et al.* (2004)

*Calculated from a total ATP concentration of 5 mM together with a free Mg^{2+} concentration of 1 mM. A Mg^{2+} affinity for ATP of 200 μM is also assumed (Bers, 2001). †Swept in numerical experiments. Assumed to be the presented value for all other experiments. This gives a total number of Ca^{2+} binding sites of 219 μmol (l cytosol) raised to -1 (Bers, 2001). ‡When CSQN is distributed in all Z-line SR compartments we keep the same total amount of CSQN as when it is only found in jSR, see Table 1 in the Supplementary Methods section. §Swept in numerical experiments. Assumed to be the same as k_{off}^{Fluo4} for all other experiments. ¶Fitted to $D_{Ca}^{cyt}/3$, together with the distance to nSR-bulk so the passive refill time constant is 212 ms (Zima *et al.* 2008).

was measured to be 1.71×10^{-12} μl, about half the size of the jSR compartment 3.78×10^{-12} μl.

In addition to the nine SR compartments we have included three intermediate SR compartments (jSRi, nSRi1, nSRi2), which are connected to the jSR and the two Z-line SR compartments at the boundaries of the whole mesh (see red lines in Fig. 1*F*). These compartments were added outside the existing compartments to improve the inflow boundary conditions into the jSR and the two Z-line SR compartments for the diffusive species included in SR (Ca^{2+} and Fluo5). Similarly, four intermediate cytosolic compartments were also added (Cytosoli [1–4]), see

Table 2. Initial values

Domains	Species	Initial value*
Cytosol	Ca^{2+}	140×10^{-3} μM
	Ca^{2+}-ATP	318×10^{-3} μM
	CaCMDN	471×10^{-3} μM
	CaFluo	2.82 μM
	CaTRPN	13.2 μM
SR	Ca^{2+}	1.3×10^{3} μM
	CaCSQN	20.1×10^{3} μM†
	CaCSQN	4.28×10^{3} μM‡
	CaFluo5	19.1 μM

*All initial values of the included buffers are assumed to be in steady state with Ca^{2+}. †When CSQN is only in jSR. ‡When CSQN is distributed in all Z-line compartments, see Table 1 in the Supplementary Methods section.

Supplementary Methods for a description of these. Also see *Diffusion fluxes* below for more details of how the geometrical parameters were chosen for the intermediate compartments.

In the rest of this paper we use *cytosolic domain* to represent the domain of the generated volumetric mesh, and *compartment* to represent a domain that is defined only with a scalar value for the volume; for example the different SR compartments. The concentration of a species found in a compartment changes with time and the value is represented by a single state variable. *Bulk compartments* represent domains containing species whose concentration does not change during the course of the simulation.

Mathematical model

The Ca^{2+} dynamics of the CRU are described by a system of reaction-diffusion equations. A system of partial differential equations (PDEs) is used to describe the dynamics in the cytosolic domain and a system of ordinary differential equations (ODEs) is used to describe the dynamics in and between the compartments. These two systems of equations are coupled through fluxes between the cytosolic domain and any neighbouring compartments. All initial values included in the model are described in Table 2.

System of partial differential equations. The system of PDEs is described by the following set of equations:

$$\left.\begin{aligned} \frac{\partial c}{\partial t} &= D_{\mathrm{Ca}}^{\mathrm{cyt}} \nabla^2 c - \sum_i R_i\left(c, cB_i\right), \\ \frac{\partial cB_i}{\partial t} &= D_{\mathrm{i}}^{\mathrm{cyt}} \nabla^2 cB_i + R_i\left(c, cB_i\right), \\ R_i\left(c, cB_i\right) &= k_{\mathrm{on}}^i c\left(B_{\mathrm{tot}}^i - cB_i\right) - k_{\mathrm{off}}^i cB_i, \end{aligned}\right\} x \in \Omega \quad (1)$$

with boundary conditions:

$$\left.\begin{aligned} \frac{\partial c}{\partial n} &= s^k J^k \\ \frac{\partial cB_i}{\partial n} &= s^k J_i^k \end{aligned}\right\} x \in \partial\Omega_k. \quad (2)$$

Here c is the $[Ca^{2+}]$ and $D_{\mathrm{Ca}}^{\mathrm{cyt}}$ the diffusion constant of Ca^{2+}. cB_i is the concentration and D_i^{cyt} the diffusion constant of the ith buffer with Ca^{2+} bound to it. i refers to ATP, CMDN (calmodulin), Fluo4 or TRPN (troponin C). See Table 1 for values of the parameters, including references, for all included species.

The total boundary, $\partial\Omega$, is divided into 17 boundaries (see Table 2 in the Supplementary Methods section). J^k and J_i^k are Ca^{2+} and buffer fluxes associated with the kth boundary (see the fifth column of Table 2 in the Supplementary Methods section). s^k determines the direction of the flux. We define our flux conventions in the same table. Fluxes in the direction Domain 1 to Domain 2 are positive. For example, s^k is '+' when the Cytosolic domain is Domain 2 and '−' when it is Domain 1. There are two different types of fluxes: diffusion and channels/transporters. There is only one boundary interfacing the cytosolic domain with diffusion fluxes, the one between the cytosolic domain and the first intermediate cytosol compartment. Fluxes on this boundary carry Ca^{2+} and mobile buffers from the cytosolic domain to the rest of the cytosol. The channels and transporters consist of the following Ca^{2+} fluxes: RyR, SERCA, NCX, Cab and pCa. Detailed definitions of all fluxes follow below.

Troponin C. TRPN is a stationary buffer so $D_{\mathrm{TRPN}} = 0$, and is excluded from the dyadic cleft. To accomplish the latter we let $B_{\mathrm{tot}}^{\mathrm{TRPN}}$ vary spatially with a sigmoidal function:

$$B_{\mathrm{tot}}^{\mathrm{TRPN}} = \frac{B0_{\mathrm{tot}}^{\mathrm{TRPN}}}{1 + e^{-\frac{d - d_{\mathrm{tt}}}{\sigma_{\mathrm{tt}}}}}. \quad (3)$$

Here d is the distance to the junctional t-tubule boundary, σ_{tt} is the sharpness of the sigmoidal function and d_{tt} is a cutoff distance to the t-tubule boundary. d is the solution to the eikonal equation:

$$|\nabla d| = 1, \quad (4)$$

with $d = 0$ enforced at the junctional t-tubule boundary. Equation (4) fixes the magnitude of the gradient of d to 1, forcing d to increase linearly with the distance from the boundary.

System of ordinary differential equations. The system of ODEs is described by the following set of equations:

$$\frac{\mathrm{d}c^n}{\mathrm{d}t} = J_{\mathrm{Ca}}^n - \sum_i R_i^n\left(c^n, cB_i^n\right), \quad (5)$$

$$\frac{\mathrm{d}cB_i^n}{\mathrm{d}t} = J_{cB_i}^n + R_i^n\left(c^n, cB_i^n\right), \tag{6}$$

$$R_i^n\left(c^n, cB_i^n\right) = k_{\mathrm{on}}^i c^n\left(B_{\mathrm{tot}}^i - cB_i^n\right) - k_{\mathrm{off}}^i cB_i^n. \tag{7}$$

Here c is the $[Ca^{2+}]$ in the nth compartment and cB_i^n is the ith buffer in this compartment. An overview of all compartments, and which species each compartment contains, is given in Table 1 in the Supplementary Methods section. J_{Ca}^n and $J_{cB_i}^n$ are the total Ca^{2+} and buffer fluxes associated with the nth compartment and they are given by:

$$J_{\mathrm{Ca}}^n = \sum_j^{N^n} s^{j,n} J_{\mathrm{Ca}}^j \mathrm{A}^j \tag{8}$$

$$J_{cB_i}^n = \sum_j^{N_i^n} s^{j,n} J_{cB_i}^j \mathrm{A}^j \tag{9}$$

Here N^n and N_i^n represent the number of Ca^{2+} and buffer fluxes associated with each compartment. A^j is the area of the boundary the jth flux crosses. The areas of all flux boundaries are given in the third column of Table 2 in the Supplementary Methods section. As for the PDE fluxes, eqns (1) and (2), each flux has a direction, $s^{j,n}$, as defined in Table 2 in the Supplementary Methods section.

Fluo5. Fluo5 is included in the model to relate changes in local SR Ca^{2+} concentrations to a corresponding fluorescence record (Shannon *et al.* 2003). We report the Fluo5 signal as F/F_0, where F is the average quantity of Ca^{2+} -bound Fluo5 in the three Z-line compartments (jSR, SRZ1 and SRZ2), and F_0 is the average Ca^{2+}-bound Fluo5 at the start of the simulation. The Z-line compartments cover a length of $\sim$1 μm, which is approximately equal to the size of the region used to register the Fluo5 signal experimentally (Zima *et al.* 2008). We use the Fluo5 signal to constrain termination of SR Ca^{2+} release, such that the nadir of F/F_0, occurs at 60% (40% depletion of F/F_0), as observed experimentally (Zima *et al.* 2008; Picht *et al.* 2011). This approach allows us to assess the timing of release termination and degree of SR Ca^{2+} depletion, while still constraining our simulations to experimental fluorescence records.

Because release termination is tied to the Fluo5 signal, our model predictions are dependent upon the dynamics of the dye. The steady state affinity of Fluo5 is assumed to be 400 μM (Shannon *et al.* 2003; Picht *et al.* 2011), but $k_{\mathrm{on}}/k_{\mathrm{off}}$ are, as far as we know, not yet determined. We therefore investigated the effect of varying k_{off} on the termination time and the jSR $[Ca^{2+}]$ after release termination. The total amount of Fluo5 within the SR, B_{tot}, is also unreported. However, we found that the termination time and SR $[Ca^{2+}]$ after release termination are independent of B_{tot} (data not shown). For all simulations presented in this study we therefore apply a value of 25 μM for B_{tot}, as has been done previously (Picht *et al.* 2011).

Calsequestrin. CSQN is the main Ca^{2+} buffer in the SR (Bers, 2001), and has recently gained attention for the possibility that it acts as a direct regulator of RyRs (Györke *et al.* 2009). We have employed a simple RyR regulatory scheme (see below) and the direct interaction between CSQN and RyR is beyond the scope of the present study. As such, we only considered CSQN for its role in Ca^{2+} storage within SR. However, through this action it controls the free SR $[Ca^{2+}]$, which is reported by Fluo5, and is itself a known regulator of RyR open probability (Györke & Györke, 1998; Laver, 2007). We hypothesized that the free Ca^{2+} level and the total available Ca^{2+} after release termination depend on CSQN localization within the fairly complex SR geometry. To test this we distributed CSQN in two ways: (i) only in the jSR compartment or (ii) evenly through all SR compartments at the Z-line. Total SR CSQN content was maintained constant between these conditions, and was equivalent to that required to achieve 25 mM in the jSR compartment alone. This equates to 219 μmol (l cytosol) raised to -1, an amount that is within the estimated range of 175–350 μmol (l cytosol) raised to -1 as calculated by Bers (2001). The value of total available Ca^{2+} in SR for this geometry is 240 μmol (l cytosol)$^{-1}$, as measured including the intermediate SR compartments, and compares well to empirically determined values (Bers, 2001). The Ca^{2+} affinity of CSQN was set to 640 μM (Shannon & Bers, 1997).

Ryanodine receptor flux. RyR flux was described by a functional model and is given by the following expression:

$$J^{\mathrm{RyR}} = O\left(c_{\mathrm{jsr}}\right)\mathrm{NO}_{\mathrm{RyR}} g_{\mathrm{RyR}}\left(c_{\mathrm{jsr}} - c_{\mathrm{cyt}}\right). \tag{10}$$

Here $\mathrm{NO}_{\mathrm{RyR}}$ is the number of open RyRs during a release, and g_{RyR} is the conductance of a single RyR. The former is set to 5, in agreement with a quantal nature of the RyR openings (Wang *et al.* 2004) and the latter is fitted so the initial current through a single RyR is 0.5 pA (Kettlun *et al.* 2003; Gillespie & Fill, 2008). $O(c_{\mathrm{jsr}})$ controls the release duration and is given by:

$$O(c_{\mathrm{jsr}}) \begin{cases} 1 : c_{\mathrm{jsr}} > f_{\mathrm{jsr}}^{\mathrm{term}} C_{\mathrm{sr}}^{\mathrm{init}} \\ 0 : c_{\mathrm{jsr}} \le f_{\mathrm{jsr}}^{\mathrm{term}} C_{\mathrm{sr}}^{\mathrm{init}} \end{cases} \tag{11}$$

Here c_{jsr} is the Ca^{2+} level in the jSR compartment and $f_{\mathrm{jsr}}^{\mathrm{term}}$ is a parameter given as a fraction of the initial $[Ca^{2+}]$ in SR, $C_{\mathrm{sr}}^{\mathrm{init}}$. The value of $f_{\mathrm{jsr}}^{\mathrm{term}}$ was fitted to constrain release such that the total Fluo5 signal is 60% of the original signal at its nadir (Zima *et al.* 2008), as described above. The RyRs will not reopen again once

c_{jsr} has reached $f_{\mathrm{jsr}}^{\mathrm{term}}\, C_{\mathrm{sr}}^{\mathrm{init}}$, which means the RyRs will stay closed for the remaining part of the simulation. The values of the included parameters are given in Table 3 in the Supplementary Methods section.

Diffusion fluxes. For a given boundary (see Table 2 in the Supplementary Methods section), diffusion fluxes, here superscripted by diff, are given by:

$$J_{\mathrm{Ca}}^{\mathrm{diff}} = D_{\mathrm{Ca}}^{\mathrm{m}} \frac{c^{\mathrm{D1}} - c^{\mathrm{D2}}}{\mathrm{d}x}$$
$$J_{cB_i}^{\mathrm{diff}} = D_{cB_i} \frac{cB_i^{\mathrm{D1}} - cB_i^{\mathrm{D2}}}{\mathrm{d}x} \qquad (12)$$

Here m is either sr or cyt depending on where the flux is found. c^{D1}, c^{D2}, cB_i^{D1} and cB_i^{D2} are the Ca^{2+} and buffer concentrations in the two domains associated with the boundary (short for Domain 1, Domain 2, see Table 2 in the Supplementary Methods section). dx is the distance between the centre of the two compartments.

The intermediate Z-line SR compartments were introduced to improve the Ca^{2+} capacity of the local SR, as the extent of the geometry is limited in the z and y directions and released Ca^{2+} can be diffusively recruited from SR outside the reconstructed geometry. This additional Ca^{2+} was taken into account with the added intermediate SR compartments. Three free parameters were added to the model for each compartment: the volume, the distance between the compartment and the neighbouring Z-line compartment (jSR, SRZ1, SRZ2), and the area between the compartments and the nSR-bulk compartment.

We applied the same value for each parameter in all three compartments. The volume was chosen to have the same magnitude as the volumes of the other Z-line compartments: $2.86 \times 10^{-12}\ \mu$l. The area was chosen to have the same magnitude as the areas between the nSR compartments and nSR-bulk: 605 nm^2. The distance was chosen to have the same magnitude as the distances between the other SR compartments: 355 nm.

The Ca^{2+} diffusion constant in the SR, $D_{\mathrm{Ca}}^{\mathrm{sr}}$, and the distance to the nSR-bulk compartment, $\mathrm{d}x_{\mathrm{nSR}}^{\mathrm{bulk}}$, determine the passive Ca^{2+} refill time constant of the SR after a release. This time constant was found to be 160 ms with intact SERCA function, and 33% larger (212 ms) when SERCA was disabled by thapsigargin (Zima *et al.* 2008). To initially define the intrinsic effects of the SR geometry upon jSR refilling rate, we swept different values of $D_{\mathrm{Ca}}^{\mathrm{sr}}$ and $\mathrm{d}x_{\mathrm{nSR}}^{\mathrm{bulk}}$, to match the SERCA-independent time constant of 212 ms. In this case the fitted values were: $D_{\mathrm{Ca}}^{\mathrm{sr}} = D_{\mathrm{Ca}}^{\mathrm{cyt}}/3$ and $\mathrm{d}x_{\mathrm{nSR}}^{\mathrm{bulk}} = 1600$ nm. These two parameters are dependent, as can be seen in eqn (12). However, it is not likely that $D_{\mathrm{Ca}}^{\mathrm{sr}}$ is larger than $D_{\mathrm{Ca}}^{\mathrm{cyt}}$, and $\mathrm{d}x_{\mathrm{nSR}}^{\mathrm{bulk}}$ must correspond to a distance to where the $[Ca^{2+}]$ in the SR is unaltered. Both our values agree with these assumptions, and interestingly, our value for $D_{\mathrm{Ca}}^{\mathrm{sr}}$ is also in agreement with that estimated by a previous study (Picht *et al.* 2011). Here our predictions supports the faster SR Ca^{2+} diffusion predicted by Picht *et al.* compared to the slower diffusion measured by Swietach *et al.* (2010).

Treating a spark as a point source, $[Ca^{2+}]$ declines by diffusion as a function of r^{-2}. If we had described the flux out of the cytosolic domain to a bulk compartment with a single diffusion flux equation, the concentration would decline linearly with r. To model the radial diffusion we introduced four extra cytosolic compartments. The choice of geometrical parameters for these compartements is described in the Supplementary Methods section.

Sarco/endoplasmic reticulum Ca^{2+} ATP-ase flux. SERCA flux was described by a simplified version of the two state SERCA model developed by (Tran *et al.* 2009). The simplifications were made to reduce computation, but did not significantly alter the turnover rate. Our model differs from the original by 4%, at most, over the relevant ranges of c_{cyt} and c_{sr}, data not shown. The simplified SERCA model is given by:

$$\alpha_1^+ = \frac{k_2^+ \mathrm{MgATP}\tilde{\mathrm{Ca}}_{\mathrm{i}}^2}{\tilde{\mathrm{H}}_{\mathrm{i}}\left(1 + \mathrm{MgATP}\left(1 + \tilde{\mathrm{H}}_1\right)\right)} \qquad (13)$$

$$\alpha_2^+ = \frac{k_3^+ \tilde{\mathrm{H}}_{\mathrm{SR}}}{\tilde{\mathrm{H}}_{\mathrm{SR}}\left(1 + \tilde{\mathrm{H}}\right) + \tilde{\mathrm{H}}} \qquad (14)$$

$$\alpha_1^- = \frac{k_2^- \left[\mathrm{MgADP}\right] \tilde{\mathrm{Ca}}_{\mathrm{SR}}^2 \tilde{\mathrm{H}}}{\tilde{\mathrm{H}}_{\mathrm{SR}}\left(1 + \tilde{\mathrm{H}}\right) + \tilde{\mathrm{H}}} \qquad (15)$$

$$\alpha_2^- = \frac{k_3^- \left[\mathrm{P_i}\right] \tilde{\mathrm{H}}_{\mathrm{i}}}{\tilde{\mathrm{H}}_{\mathrm{i}}\left(1 + \mathrm{MgATP}\left(1 + \tilde{\mathrm{H}}_1\right)\right)} \qquad (16)$$

$$\nu_{\mathrm{cycle}} = \frac{\alpha_1^+\alpha_2^+ - \alpha_1^-\alpha_2^-}{\alpha_1^+ + \alpha_2^+ + \alpha_1^- + \alpha_2^-} \qquad (17)$$

$$J_{\mathrm{SERCA}} = 2\mathrm{S}_{\mathrm{SERCA}}\rho_{\mathrm{SERCA}}\, V_{\mathrm{cyt}}\mathrm{toA}_{\mathrm{sr}}\, \nu_{\mathrm{cycle}} \qquad (18)$$

Here all parameters described in eqn (13)–(16) are given in (Tran *et al.* 2009), with the exception that we have changed the temperature to 22°C. V_{cyt} to A_{sr} is the cytosolic volume to SR area ratio and is computed by:

$$V_{\mathrm{cyt}}\,\mathrm{to}\,A_{\mathrm{sr}} = \frac{V_{\mathrm{cyt}}^{\mathrm{frac}}}{A_{\mathrm{jsr}}\,\mathrm{to}\,V_{\mathrm{cell}}\frac{V_{\mathrm{nsr}}^{\mathrm{frac}} + V_{\mathrm{jsr}}^{\mathrm{frac}}}{V_{\mathrm{jsr}}^{\mathrm{frac}}}} \qquad (19)$$

The value of $V_{\mathrm{cyt}}\,\mathrm{to}\,A_{\mathrm{sr}}$ was 307 nm, which is close to the measured value from the generated geometry: 346 nm. This results in 1.3 SERCA pumps per 100 nm^2, which is reasonable based on the packing limit imposed by the

size of the SERCA protein, which is ∼4–6 nm across depending on what state it is in (Toyoshima, 2008). S_{SERCA} is a scaling parameter, which was fitted such that the refill time constant after a release, as measured by Fluo5, corresponded to the experimentally measured value of 160 ms (Zima *et al.* 2008). The fitted values for S_{SERCA} were 1.5 for CSQN distributed in Z-line SR, and 2.5 for CSQN concentrated in jSR. Note that a value of 1 implies no scaling, and corresponds to a SERCA density determined only by the geometry, the SERCA model, the volume density, the computed cytosolic volume to SR area ratio (V_{cyt} to A_{sr}), and the experimentally measured refill rate. As such, the fitted scale parameter can be seen as a free parameter, which scales one or several of the fixed parameters. Considering the number of fixed parameters and some uncertainty surrounding their ascribed values, 1.5 and 2.5 are remarkably close to 1. The parameter values used for the SERCA flux, which are not described in Tran *et al.* (2009), are given in Table 3 in the Supplementary Methods section.

Labelling studies suggest that SERCA is not distributed evenly throughout the sarcomere (Bidwell *et al.* 2011), but more concentrated at the Z-line. Where SERCA is included in our model, we distributed it evenly at the SR membranes. However, because the Z-line SR compartments are much larger (see Fig. 1*F*), the apparent concentration of the SERCA will be larger at the Z-line.

We hypothesized that incorporating the SERCA pump within the CRU domain will prolong release. During the release Ca^{2+} is pumped back into SR, thereby delaying the depletion of Ca^{2+} in the jSR, which in our model, will prolong release. To test if this was the case we compared release termination for different SERCA distributions: (i) without any SERCA, (ii) with SERCA applied to all SR boundaries with the exception of the jSR compartment, and (iii) SERCA applied to the boundaries in (ii) together with the Back boundary of the jSR.

We also measured how much Ca^{2+} could be pumped into the SR via SERCA from a Ca^{2+} wave-front arriving at the CRU. This measurement is a rudimentary proof-of-principle test for how effectively a Ca^{2+} wave-front can sensitize the RyRs in the CRU via increased SR Ca^{2+} load (Keller *et al.* 2007). The distance between the CRUs in the longitudinal direction was ∼2 μm and with a Ca^{2+} wave travelling at 100 μm s^{-1} (Lamont *et al.* 1998; Ter Keurs & Boyden, 2007), each CRU should recruit the next at roughly 20 ms intervals. Therefore we fixed the Ca^{2+} in the cytosolic domain to values representative of an arriving Ca^{2+} wave-front, and measured the Ca^{2+} level in the jSR over 20 ms.

t-Tubule fluxes. At the t-tubule boundaries we include three different fluxes. The NCX, the sarcolemmal Ca^{2+} pump (pCa) and a background Ca^{2+} flux (Cab). Detailed descriptions of the equations used to model these three fluxes are given in the Supplementary Methods section.

Localization of NCX is likely to be very important to its role in myocardial Ca^{2+} handling, particularly if as previously suggested (Trafford *et al.* 1995; Lines *et al.* 2006) NCX exists within the dyad where it would experience a very high local [Ca^{2+}]. We hypothesized that including NCX flux within the dyad would be capable of directly and markedly altering dyadic [Ca^{2+}], and spark dynamics. We tested this hypothesis by comparing simulations for which the t-tubule fluxes were either included or excluded from the dyad.

Linescan generation

To compare the size of the generated spark to experimental observations we computed a linescan image based on the F/F_0 signal of the included Fluo4. Because the generated geometry is too small to be used directly in this calculation, we applied the method previously described by Smith *et al.* (1998) to reconstruct a linescan image of the spark. This was done by recording the release current from a full simulation of our model, and applying this as a point source to the PDE, as described above. Owing to radial symmetry the problem is effectively one-dimensional. The resulting F/F_0 signal was then integrated at the linescan integration points, using a Gaussian kernel, with previously reported parameters (Smith *et al.* 1998). White noise is added to the resulting image to mimic experimental conditions.

Numerical software

To solve and store the results from the coupled system of ODEs and PDEs, we developed a dedicated software package, SubCell. The software is free and can be downloaded from launchpad (launchpad.net/subcell). SubCell is developed in Python and takes declarative model files, similar to Virtual Cell (Moraru *et al.* 2008), but for finite element problems, and without input from a graphical user interface. SubCell utilizes components from the FEniCS project (Logg *et al.* 2012), which is a collection of free software for automated and efficient solutions of differential equations. All files needed to run the simulations presented in this study, including the generated geometry, can be obtained by contacting the corresponding author.

Results

Local Ca^{2+} gradients are large during a spark

The basic characteristics of a Ca^{2+} spark are shown in Fig. 2. All data are from the same simulation, in

which CSQN was distributed throughout the Z-line SR compartments, and all other parameters were as provided in Methods. A volumetric representation of the Ca^{2+} concentration in the cytosolic domain (after 5 ms) reveals the large Ca^{2+} gradients surrounding the CRU (Fig. 2*A*, and the movie in the online Supplemental Material). Comparing $[Ca^{2+}]$ at the jSR Back boundary, in the whole cytosolic domain, and at the 6th nSR compartment (Fig. 2*B*), we see that the $[Ca^{2+}]$ peaks at roughly 5 μM at the back of the jSR. If SERCA is localized to this boundary, it senses a high $[Ca^{2+}]$. On the other hand, SERCA at the 6th nSR compartment (the M-line) senses

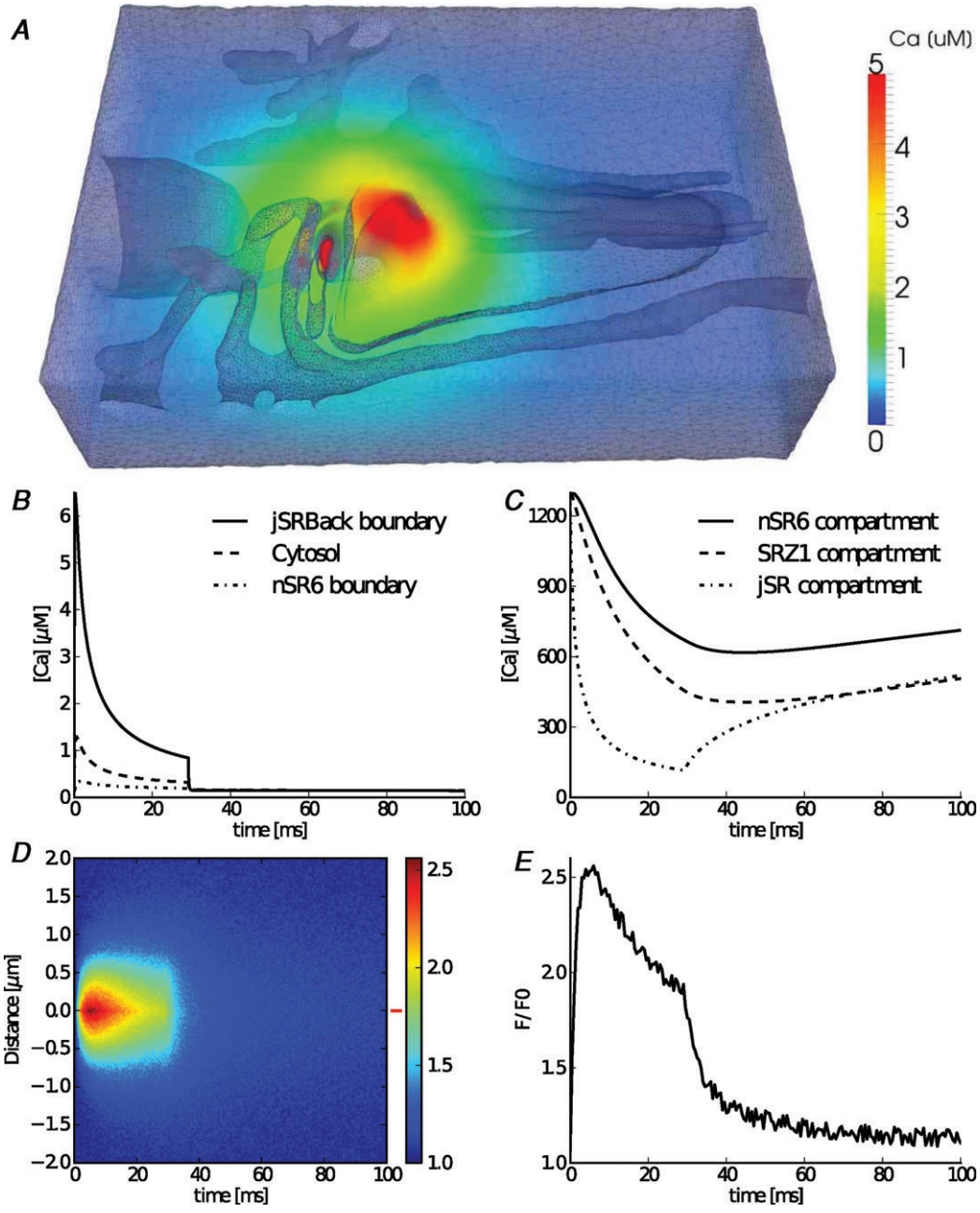

Figure 2. Ca^{2+} characteristics
A, a volumetric representation of the $[Ca^{2+}]$ in the cytosol domain after 5 ms. *B*, the average $[Ca^{2+}]$ at three different positions: backside boundary of jSR (continuous line), the whole cytosolic domain (dashed line), and at the boundary of the 6th nSR compartment (dash-dotted line). *C*, the free Ca^{2+} content in three SR domains during a spark: the 6th nSR compartment (continuous line), the 1st Z-line SR compartment (dashed line), and the jSR compartment (dash-dotted line). *D*, a generated line-scan image from the Fluo4 signal with added noise. The FWHM is 1.0 μm and the FDHM is 28.5 ms. *E*, a Fluo4 trace from the red marker at the right of the line-scan image.

a peak that is 17-fold smaller (0.3 μM), illustrating the potential significance of SERCA localization during a spark. These local values should also be compared with the average [Ca^{2+}] in the cytosolic domain, which peaks at 1.1 μM, and rapidly equilibrates with the [Ca^{2+}] in the bulk cytosol, 0.14 μM. The relative Ca^{2+} gradients are smaller in SR than in the cytosolic domain, even though diffusion in the SR is much slower than in the cytosol (see Fig. 2*C*). The jSR [Ca^{2+}] concentration reaches its nadir of 120 μM after 19 ms, whereas the nSR6 and SRZ1 [Ca^{2+}] reach their respective nadirs much later. This is because directly after release termination, a larger amount of Ca^{2+} re-binds to CSQN than is immediately refilled via SERCA activity and diffusion from the nSR-bulk compartment. The generated linescan image can be seen in Fig. 2*D*. The width and duration of the spark (FWHM = 1.0 μm, FDHM = 28.5 ms), compares well with corresponding experimental measures (Maier *et al.* 2003). A Fluo4 trace extracted from the red marker in Fig. 2*D* is shown in Fig. 2*E*.

Locality of CSQN determines the actual release termination based on Fluo5 signal

The release termination in our model was fitted so that the nadir of the Fluo5 signal was 60% of its initial strength (Zima *et al.* 2008). To find the timing of the release termination we used a simplified version of the model, with SERCA and t-tubule fluxes excluded. As we will see below, the timing of release termination does depend on SERCA, but for the purpose of illustrating the correlation between the release termination and the nadir of Fluo5, we do not include SERCA in the following simulations.

We first observe that the kinetics of Fluo5 cause its reported fluorescence to lag changes in SR Ca^{2+}, and thereby substantially overestimate SR Ca^{2+} load at all times after release has been initiated, see Fig. 3*A*. This is most evident in the jSR, which after 10 ms only contains 20% (for distributed CSQN) or 30% (for concentrated CSQN) of its initial Ca^{2+} content, while at the same instant Fluo5 reports 80% of its initial fluorescence. Secondly, when CSQN is concentrated in the jSR, we observe that total SR Ca^{2+} is drained much more rapidly than when CSQN is distributed throughout the Z-line SR compartments. This is because a larger jSR Ca^{2+} pool permits the Ca^{2+} gradient across the SR membrane to be better maintained during the period of release, and hence slows decay of the release current (see panel *B*). This is also evident in the decay of total SR Ca^{2+} (dashed lines), which declines much faster when CSQN is concentrated. Naively we could use these traces to determine the spark termination time as the time when the Fluo5 signal reaches 60% of its initial value, as reported by experiments. By following the thin dashed line these timings would be 23.0 ms for the concentrated CSQN and 28.3 ms for the distributed CSQN. However, as in Fig. 2*C*, because CSQN is a large sink for Ca^{2+} returning to the jSR, the local free Ca^{2+} continues to decline after release is terminated. Thus, the Fluo5 signal also continues to decline, such that if we had terminated the release at these timings, the Fluo5 nadir would have exceeded the experimentally observed 60%. To avoid errors due to differences in this post-release decline of jSR free Ca^{2+} and fluorescence, we fitted the release termination for both distributions of CSQN, so that the true nadir of the Fluo5 signal ocurred at 60% of its initial value (see Fig. 3*C*). We then obtained earlier terminations compared with the naively determined termination times from Fig. 3*A*, and we also noticed that termination occurs much earlier for the runs with concentrated than distributed CSQN (15.1 ms *versus* 24.5 ms). This exaggeration occurs because CSQN depletion was more complete when it was concentrated than distributed, and subsequently it takes longer to replete after release termination. The nadir of Fluo5 was 36.9 ms when CSQN was concentrated and 31.8 ms when it was distributed. The total available Ca^{2+} in all SR compartments, as reported by the dashed line, was quite large after a release termination: 37% for concentrated CSQN and 44% for distributed CSQN, but much lower (18% when concentrated, and 9% when distributed) in the jSR alone. In Fig. 3*D* are shown the total release currents for the two different runs. By integrating the release flux we obtain a total of 39,200 Ca^{2+} ions released when CSQN was concentrated and 35,500 ions when CSQN was distributed.

The computed release termination depends on the kinetic properties of Fluo5 (Fig. 4*A*), which are difficult to establish *in vivo*. For all values of k_{off}^{Fluo5}, release termination occurred earlier when CSQN was concentrated in the jSR, and that release termination time was only sensitive to changes in k_{off}^{Fluo5} at values less than 0.5 ms^{-1}. The k_{off}^{Fluo5} value assumed for all other simulations (0.1 ms^{-1}) is in this range, and therefore caused the model to be quite sensitive to variation in this parameter. In the absence of a well-defined k_{off}^{Fluo5}, our main reasons for adopting this value are for consistency with key reference data sets (Picht *et al.* 2011), and similarity to the established k_{off}^{Fluo5} of the closely related Fluo4.

A second finding is that release termination time is more sensitive to k_{off}^{Fluo5} when CSQN is distributed, which indicates that the Fluo5 report of SR [Ca^{2+}] is more sensitive to dye kinetics for this CSQN distribution. To explain this result we divide the Fluo5 reaction into two different phases: (i) release (between release start and release termination), and (ii) refill phase (between release termination and the Fluo5 nadir). In the release phase the Fluo5 reaction is reaction dominated, as the dye struggles to keep pace with the rapidly decreasing [Ca^{2+}], whereas in the refill phase the Ca^{2+} dynamics is slow, determined by re-sequestering of Ca^{2+} to CSQN and passive diffusion

from nSR bulk, and the reaction is therefore diffusion dominated. A change in k_{off}^{Fluo5} would only be capable of altering the Fluo5 signal when Ca^{2+} binding is reaction dominated, which it is during the release phase. The release phase is much longer when CSQN is distributed (~60% longer compared to when CSQN is concentrated), and we hypothesize that this time difference is the main cause for the higher k_{off}^{Fluo5} sensitivity for distributed CSQN.

The available Ca^{2+} in SR after a release is dependent on the release termination. When the spark is open longer, due to lower values of k_{off}^{Fluo5}, the SR should get comparably more depleted. It is therefore somewhat counterintuitive that SR Ca^{2+} level after release termination follows a more blunt curve, compared to the release termination curve, especially for the distributed CSQN. This can, however, be explained by the comparably small release current for the late part of the release when CSQN is distributed.

As expected, in Fig. 4*C* we see a positive correlation between the amount of Ca^{2+} available throughout the SR compartments (represented by the total CSQN), and termination time. These alterations in termination time are not accompanied by large differences in the Ca^{2+} availability at termination, although a slight increase in the total available Ca^{2+} (stars) is present (Fig. 4*D*).

The spark termination time is also dependent on D_{Ca}^{sr}. In Fig. 2 in the Supplementary Results section, we see that when CSQN is distributed the termination time gets longer with faster SR diffusion. This is because a higher jSR $[Ca^{2+}]$ was sustained, which prolonged the spark. Note, however, that the refill time constant is 212 ms only when $D_{Ca}^{sr} = D_{Ca}^{cyt}/3$.

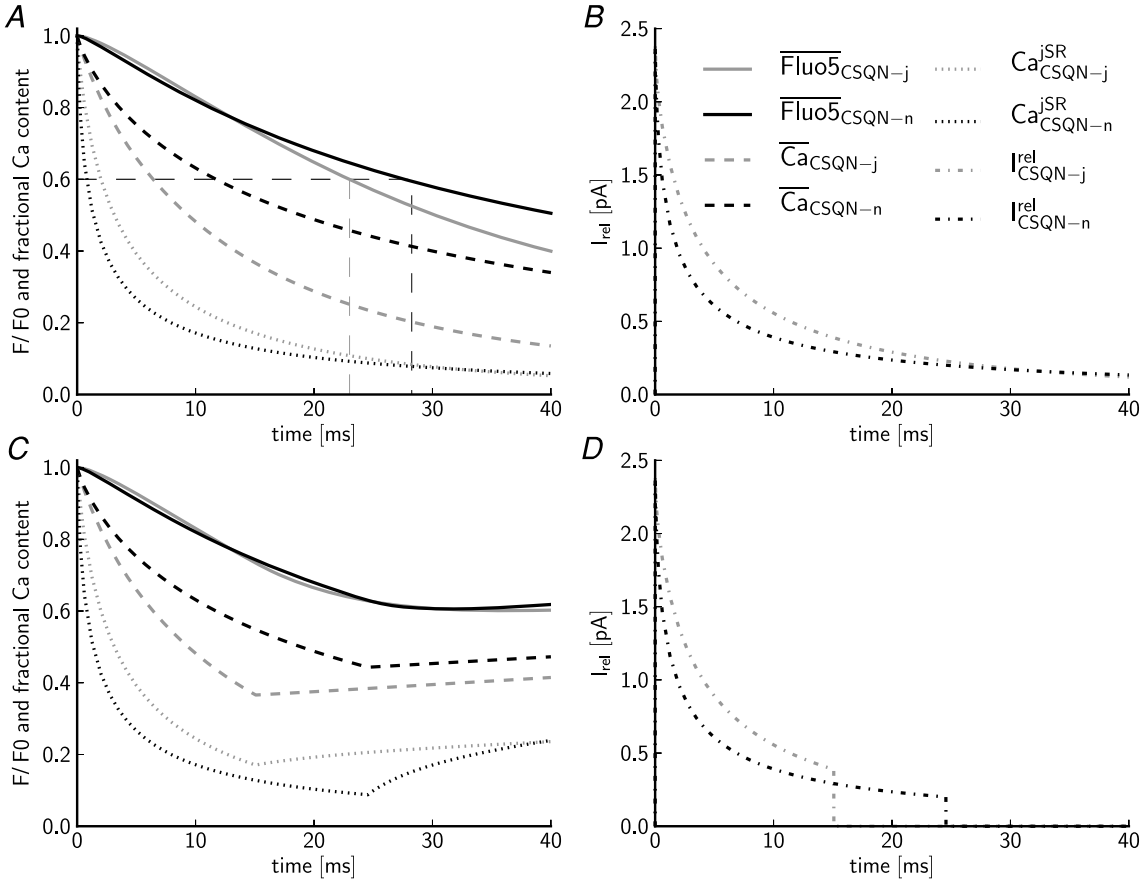

Figure 3. Ca^{2+} depletion levels in SR during release
For all panels in this figure the grey lines represent data where CSQN is concentrated in jSR, and the black lines data where CSQN is distributed across all Z-line SR compartments. *A*, the local Fluo5 F/F_0 signal (continuous lines). Assuming a naive release termination at 60% of the original Fluo5 signal, the thin long dashed lines report the release termination time where they cross the *x*-axis; 23.0 ms for CSQN in jSR and 28.25 ms for CSQN distributed across Z-line nSR. Total available Ca^{2+} in all SR compartments, including Ca^{2+} bound to CSQN (dashed lines). The free Ca^{2+} in the jSR compartment (dotted lines). *B*, the total release current. *C*, the same traces as in *A*), but now with a release termination fitted so the nadir of the local Fluo5 level reaches 60%. The termination times and the Fluo5 nadir times are: 15.1 ms and 36.7 ms for CSQN in jSR and 24.5 ms and 31.8 ms for CSQN distributed across Z-line nSR. *D*, the total release currents when release termination is included. The integrated number of released Ca^{2+} are: 39,200 for CSQN in jSR and 35,500 for CSQN distributed across Z-line nSR.

SERCA pump increases release termination time

In Fig. 5*A* are the purely diffusive 'passive' (dashed) and SERCA augmented (continuous) SR refilling rates illustrated by the corresponding Fluo5 signals. The passive rate was first fitted to achieve a 212 ms time constant for refilling. Then SERCA flux was included and its strength (S_{SERCA}) was fitted to decrease the time constant to 160 ms. This result is in close agreement with model results in which increased SERCA activity was simulated to result from β-adrenergic stimulation (Ramay *et al.* 2011). Although their index of jSR $[Ca^{2+}]$ is subtly different to the Fluo5 fluorescence shown in Fig. 5*A*, the qualitative effects of SERCA activity on jSR refilling are very similar. The actual $[Ca^{2+}]$ follows a slightly slower time course than the Fluo5 signal, as is illustrated in Fig. 2 in the Supplementary Results section. Even if SERCA was added, most Ca^{2+} escaped to Cytosol. During the spark only 21% of the total released Ca^{2+} was pumped back, corresponding to experimentally measured values (Gómez *et al.* 1996).

First and foremost, we observe prolonged release when SERCA is added to the SR boundaries (Fig. 5*B*). When SERCA was included everywhere except at the back of the jSR, the termination time increased by 2.7 ms for a distributed CSQN profile, and 1.0 ms for concentrated CSQN. The corresponding fractional increases were 11% and 6.3%, respectively. When SERCA also was included directly at the back of the jSR, release termination was further prolonged – to 4.7 ms when CSQN was distributed and to 1.5 ms when it was concentrated, with the corresponding fractional increases of 20% and 10%, respectively. We saw a smaller increase when CSQN is concentrated in the jSR. This is because the free $[Ca^{2+}]$ is lower in the SR in general, and in the jSR in particular, when CSQN was distributed throughout the Z-line. The lower Ca^{2+} concentration creates a lower Ca^{2+} gradient that opposes SERCA.

While the release duration is prolonged by SERCA, the net Ca^{2+} may not be altered because Ca^{2+} is being

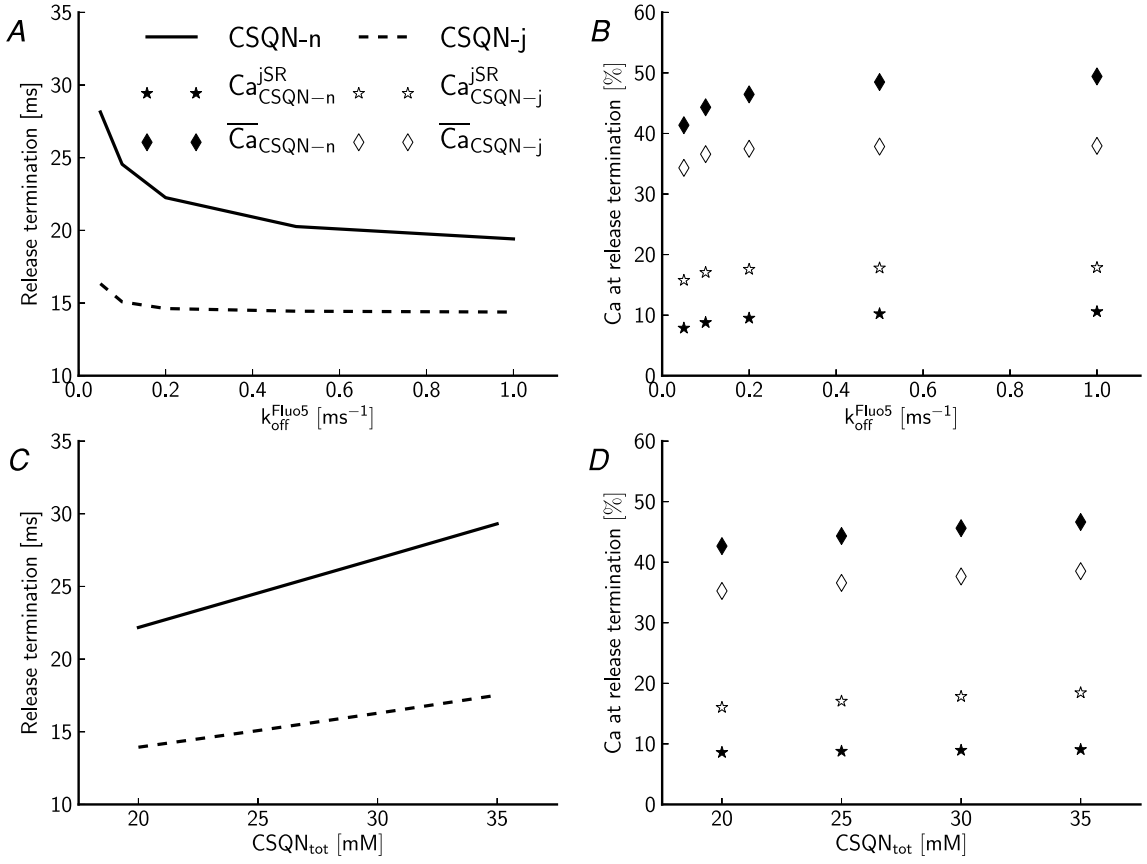

Figure 4. Ca^{2+} levels at release termination
Dashed lines and open symbols represent data where CSQN is concentrated in jSR, and continuous lines and filled symbols represent data where CSQN is distributed across all Z-line SR compartments. *A*, the release termination time as a function of Fluo5 dynamics (k_{off}). *B*, free Ca^{2+} in jSR (stars) and total available Ca^{2+} (including Ca^{2+} bound to CSQN) in all SR compartments (diamonds), at the time of release termination, as a function of Fluo5 dynamics (k_{off}). *C*, the release termination time as a function of the amount of total CSQN within the local SR. *D*, free Ca^{2+} in jSR (stars) and total available Ca^{2+} (including Ca^{2+} bound to CSQN) in all SR compartments (diamonds), at the time of release termination, as a function of total CSQN within the local SR.

actively removed from the cytosolic domain. In fact, the net released Ca^{2+} decreased by 1000 ions, when SERCA was added and CSQN was concentrated (see Fig. 5*C*). The decrease was 500 ions less when SERCA was also added to the back of jSR. However, when CSQN was uniformly distributed, the inclusion of SERCA increased net Ca^{2+} release by 2200 ions, and 4500 ions when SERCA was also added to the back of jSR – a relative increase of 12%.

In the final panel, Fig. 5*D*, we estimate how much jSR $[Ca^{2+}]$ increases as a result of elevated cytosolic $[Ca^{2+}]$, and hence how readily an approaching Ca^{2+} wave-front could promote spontaneous release by enhancing SR Ca^{2+} load, as previously hypothesized (Keller *et al.* 2007). From the scenario with the largest increase of cytosolic $[Ca^{2+}]$ (0.56 μM), $[Ca^{2+}]$ in the jSR increased by 2% over the 20 ms of simulation. The presented values were recorded when CSQN was distributed. A 3% change was achieved when CSQN was concentrated (data not shown). This increase was caused solely by the higher S_{SERCA} value when CSQN was concentrated, as all other variables and parameters were the same.

NCX fluxes in the dyad do not alter the local Ca^{2+} concentration

The cytosolic Ca^{2+} profile during a spark is not altered significantly by including NCX within the dyad. Figure 6*A* shows the average cytosolic $[Ca^{2+}]$ during a spark with and without including NCX in the dyadic t-tubule membrane. The maximal difference between these two scenarios was 2%. The same trend can be seen for the local $[Ca^{2+}]$ within the dyad (Fig. 6*B*), where the maximal difference was only slightly larger, 3%, even though peak Ca^{2+} reached a much higher level in this restricted domain. Based on an average NCX distribution of 400×10^{-6} nm^{-1} (Bers, 2001), and the surface area of our t-tubular geometry, we estimate that about 41 NCX molecules should be located at the

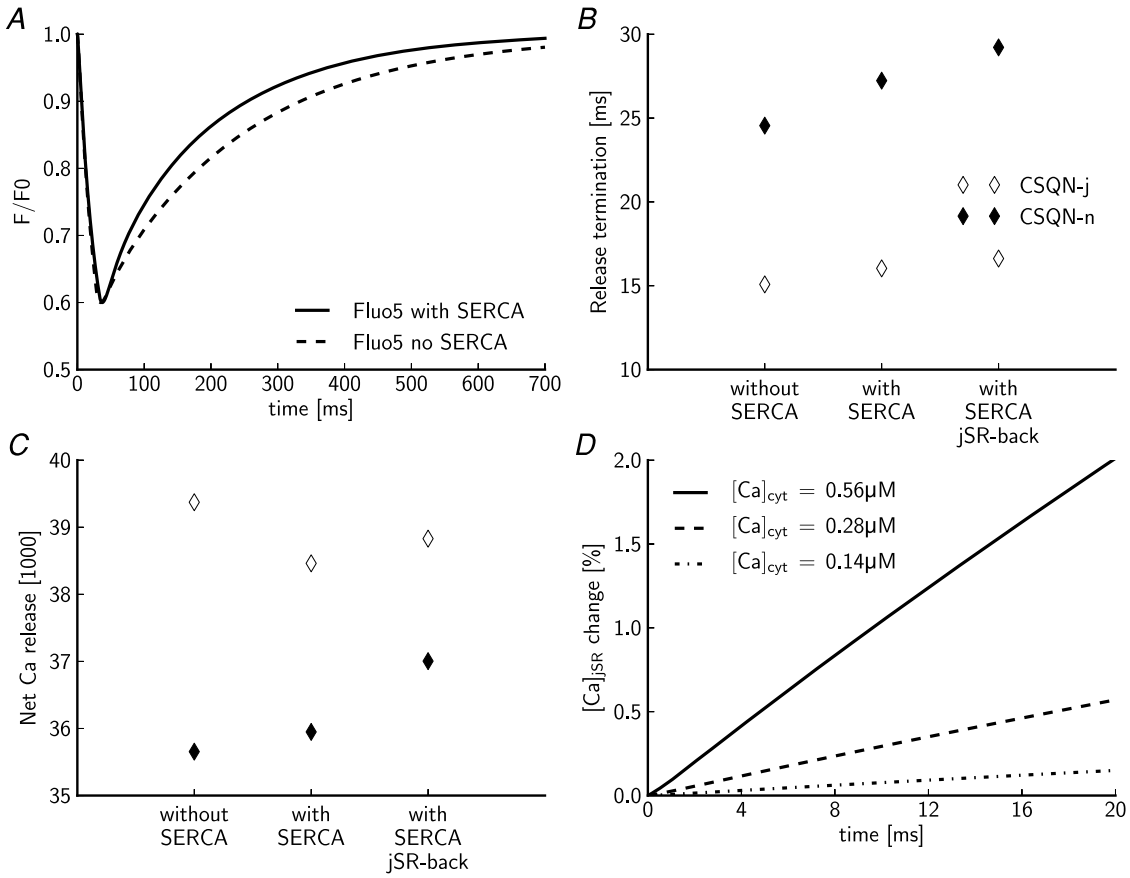

Figure 5. Local SERCA pump effect
A, the SR Ca^{2+} refill times were fitted so the time constant for restitution of the local Flou5 signal was 160 ms with SERCA and 212 ms without SERCA (Zima *et al.* 2008). *B*, release termination time as a function of SERCA inclusion and SERCA position. The open symbols represent release times where CSQN is concentrated in jSR, and filled symbols represent data where CSQN is distributed across all Z-line SR compartments. *C*, net Ca^{2+} released from SR (released Ca^{2+} minus Ca^{2+} re-uptaken by SERCA) as a function of SERCA inclusion and SERCA position. *D*, SERCA induced Ca^{2+} change in jSR for different fixed cytosolic Ca^{2+} values.

junctional boundary, with another 38 spread over the rest of that t-tubule surface (TT2). The average currents passing through one NCX at these two boundaries peaked at 0.2 fA for the NCX in the junction and at 0.1 fA for the remaining t-tubule boundary (Fig. 6*C*). These values are well within the theoretical maximal unitary current of 0.8 fA, which is computed based on a maximal turnover rate of 5 ms^{-1} (Bers, 2001).

Discussion

Geometry

Reaction–diffusion models are now commonly used to study subcellular signalling, but the effects of the complex three-dimensional geometry of microdomains such as the CRU have typically not been investigated in sub-cellular models. Using a realistic geometry we were able to minimize uncertainties related to the spatial relationship between the interacting organelles of the CRU, particularly with respect to CSQN localization and the local effects of the SERCA pump. Additionally, models assuming a continuous distribution of the SR volume induce systematic errors with respect to the relative Ca^{2+} capacity of the SR (Swietach *et al.* 2010; Picht *et al.* 2011). In our reconstructed geometry it is evident that SR compartments close to the Z-line have a greater Ca^{2+} capacity than those close to the M-line. This greater local Ca^{2+} capacity at the Z-line maintains a Ca^{2+} gradient that contributes importantly to Ca^{2+} release dynamics during a spark. Finally, using a realistic geometry not only incorporates more realistic sizes and connectivities of the SR compartments, but also appropriately relates the SR membrane, and its incorporated transport mechanisms, to the cytosolic domain. The local Ca^{2+} handling proteins such as RyRs, SERCA and CSQN all experience steep local $[Ca^{2+}]$ gradients, which need to be resolved in a proper manner.

Dynamic movement of Ca^{2+} within or into the SR

Dynamic movement of Ca^{2+} within the SR plays a key role in several physiological processes in cardiomyocytes, as recently reviewed by Sobie & Lederer (2012). In this study, we have used a reconstructed geometry of a CRU to address several aspects of local Ca^{2+} movements within the SR during a spark: (i) Ca^{2+} depletion in the junctional and surrounding SR structures, (ii) intra-SR distribution of CSQN and its effect on spark termination, and (iii) the ability of local SERCA activity to dynamically prolong spark duration.

Severe junctional Ca^{2+} depletion is reconcilable with a higher regional Ca^{2+} reserve after a spark. Experimental studies suggest that a considerable amount of Ca^{2+} is available for release after a spark has terminated (Shannon *et al.* 2000*a*; Zima *et al.* 2008). Recently, several studies using Fluo5 as a Ca^{2+} indicator within the SR have reported 40% local depletion of the SR Ca^{2+} store during a spark (Zima *et al.* 2008; Picht *et al.* 2011). This stands in contrast to predictions from model studies, which have consistently suggested a much larger local depletion of ~90% (Sobie *et al.* 2002; Ramay *et al.* 2010; Williams *et al.* 2011). Importantly, changes in $[Ca^{2+}]$ reported by the Fluo5 signal incorporate both the true changes in free $[Ca^{2+}]$, and the temporal characteristics of the dye. To access

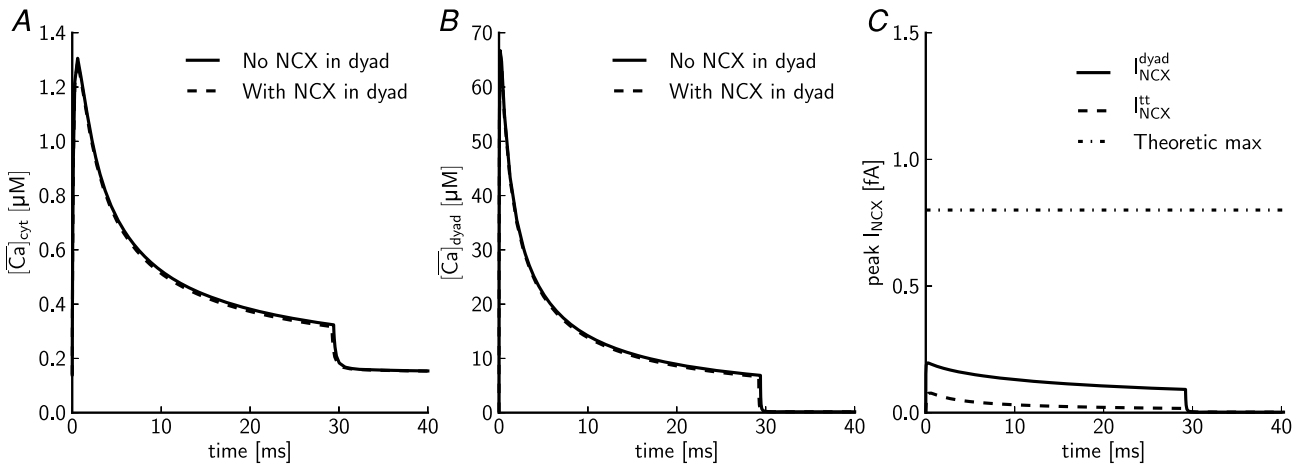

Figure 6. NCX in the dyad
A, average Ca^{2+} levels in the cytosolic domain when NCX is included in the dyad (continuous line) and when the NCX is not included (dashed line). *B*, average Ca^{2+} levels at the t-tubule boundary within the dyad when NCX is included in the dyad (continuous line) and when the NCX is not included (dashed line). *C*, current from a single exchanger from within the dyad (continuous line) and from the adjacent t-tubule boundary (dashed line). The theoretical maximal exchange current is 0.8 fA (dash-dotted line).

the true free [Ca^{2+}] at any instant, this signal needs to be deconvolved. Also, as suggested by Sobie & Lederer (2012), the spatial resolution of the fluorescence signal prevents recordings of [Ca^{2+}] from the jSR only. In this study, we not only correlate the actual Ca^{2+} levels of SR to the corresponding dye signal, but also base our criterion for release termination upon the average Fluo5 signal from a region larger than just the jSR. The size of the region we chose is similar to that used in the experimental studies, $\sim$1 μm.

Independent of where CSQN is distributed, we see that the Ca^{2+} content of the jSR depletes rapidly, and to a very low level. Even though our model of spark termination is rudimentary and only depends on a fitted nadir of the Fluo5 signal (to 60% of its initial value), it predicts a very low jSR [Ca^{2+}] after spark termination. Simultaneously, the amount of available Ca^{2+} throughout the regional SR domains after a release is much higher than that available in the jSR, and corresponds roughly to an experimentally measured fractional release of 35–50% (Antoons *et al.* 2002). We propose that these data reconcile the apparent difference between existing experimental data and earlier computational predictions.

Distribution of CSQN determines release termination. We also investigated how the distribution of CSQN affects the termination of a spark. It has generally been reported that CSQN colocalizes with RyR, both functionally and structurally (Györke *et al.* 2004; Franzini-Armstrong *et al.* 2005; Lukyanenko *et al.* 2007). However the potential for it to be localized within the SR compartments adjacent to and contiguous with the terminal cisternae is less fully investigated and not well established. Early studies involving immune-labelling of calsequestrin in thin-section transmission electron microscopy show pronounced labelling of three compartments distinguished as the peripheral and interior forms of jSR, and corbular SR (Jorgensen *et al.* 1985, 1993). The peripheral jSR and interior jSR probably represent similar terminal cisternal compartments, at which triggered Ca^{2+} release occurs, the only difference being that the interior form abuts the t-tubular rather than surface sarcolemmal membrane. The corbular SR is likely to represent a distinct compartment, because while it occurs primarily at the Z-line, it does not juxtapose a sarcolemmal membrane (Jorgensen *et al.* 1985, 1993; Asghari *et al.* 2009). The functional role of these so-called corbular SR structures remains unclear, but has received considerable attention for their potential involvement in the EC decoupling that occurs in heart failure (Song *et al.* 2006). Looking at the shape of SRZ1 and SRZ2, and to a certain extent nSR1, it is natural to relate these SR compartments to prior descriptions of corbular SR morphology (Dolber & Sommer, 1984; Franzini-Armstrong *et al.* 2005). Therefore, we chose to investigate the functional impact of uniformly distributing CSQN among these compartments, as an alternative to concentrating it solely within the junctional SR. While we cannot conclude from our results whether or not CSQN is uniformly distributed, we do see clear differences in behaviour for different CSQN distributions, especially an earlier release termination when CSQN is concentrated in the jSR.

We first observed that the free [Ca^{2+}] in the jSR decreased faster during a spark when CSQN was uniformly distributed. This is because the lower local CSQN confers a proportionally lower local Ca^{2+} reserve. By the same mechanism, the distributed CSQN profile is less able to maintain a high Ca^{2+} gradient with respect to the cytosol and hence results in a smaller release current. The smaller release current drains Ca^{2+} from the SR more slowly. When release termination was not included, these differences in release flux caused the Fluo5 signal to reach 60% of its initial value more slowly when CSQN was uniform than when CSQN was concentrated in the jSR. However, when we constrain spark termination such that Fluo5 nadir occurs at 60%, we see that this nadir is reached at more or less the same time for both CSQN distributions. This is because the free Ca^{2+} level keeps declining after a release as Ca^{2+} rebinds to CSQN. Because of the internal Ca^{2+} gradient of SR during release, with lower free Ca^{2+} in jSR compared to the other compartments, CSQN is much more depleted when it is concentrated in jSR. The more extensive CSQN depletion for jSR concentrated CSQN explains why the Fluo5 signal continues decreasing for a much longer time. So even though our model predicts a much earlier termination of the spark when CSQN is concentrated in jSR, it predicts that the nadir in Fluo5 should be similar for the two different CSQN distributions. As such, differences in CSQN distribution may have meaningful effects upon spark dynamics that are not discernable by current fluorescence techniques.

The exact localization of CSQN has not been the topic of much discussion in the modelling literature. In published models, CSQN is often only localized in the jSR compartment (Ramay *et al.* 2010), or distributed evenly throughout the whole SR (Swietach *et al.* 2010). Picht *et al.* (2011) distributed CSQN in the SR compartments closest to the Z-line, however they did not include a proper relative size of the SR compartment volumes and the resolution of the SR compartments are also relatively coarse. Our results predict that spark dynamics studies, which use RyR models that rely on a luminal [Ca^{2+}], will report different spark characteristics dependent on the distribution of CSQN.

Predicting release termination. Release termination was back calculated from the nadir of the Fluo5 signal. This causes release termination to be dependent on the

dynamics of Fluo5. We altered the k_{off}^{Fluo5} to see how sensitive termination time is to uncertainty in this parameter. In Fig. 4*A* we show that if the off-rate of the dye is faster than 0.4 ms^{-1} the release termination is more or less independent of the dye kinetics, because at this speed the dye directly follows the Ca^{2+} concentration. We have chosen to use the same value for k_{off}^{Fluo5} as for k_{off}^{Fluo4}, which is 0.1 ms^{-1}. This means that our model is sensitive to the true value of k_{off}^{Fluo5}. Further characterizations of Fluo5 dynamics are needed to better understand how they may impact experimental reports of SR Ca^{2+} dynamics.

Figure 4*C* shows that the termination time is dependent on the total amount of CSQN. This is not surprising, as a CRU with a larger CSQN content can sustain a longer spark before luminal depletion triggers termination. The relative quantity of Ca^{2+} remaining in the SR at the time of spark termination is more or less independent of CSQN content (see Fig. 4*D*). This is also to be expected, given that our release termination criteria are defined in fractional terms. A more mechanistic definition for release termination may permit alterations in total SR CSQN content to alter the residual SR Ca^{2+} content, particularly if CSQN is capable of directly regulating RyR (Györke *et al.* 2009).

SERCA pump can enhance wave propagation speed by prolonging the spark

SERCA has been suggested to play a role in enhancing Ca^{2+} wave speed dynamically (Keller *et al.* 2007). When a Ca^{2+} wave arrives at a CRU, SERCA pumps Ca^{2+} into the local SR, which may be capable of promoting release from that CRU by sensitizing the local RyRs. However, with an already high local SR $[Ca^{2+}]$, and a propagating wave-front that provides a lower local peak $[Ca^{2+}]$ than would occur during a spark, the possible SERCA current is limited by opposition from a considerable thermodynamic gradient (Shannon *et al.* 2000*b*; Tran *et al.* 2009). In a crude experiment we measured the possible effect of a sensitization front, and observed only a slight increase, 2–3%, in luminal $[Ca^{2+}]$ over a time course of 20 ms.

An alternative or complementary hypothesis for the mechanism by which SERCA enhances Ca^{2+} wave speed is suggested by our results regarding spark termination. We observed that local SERCA activity prolongs the spark by pumping released Ca^{2+} back into the SR during the spark, hence reducing luminal depletion and prolonging the release. In this scenario SERCA senses both a lower Ca^{2+} level in SR (during the second half of the release, less than 20% of initial $[Ca^{2+}]$ in jSR) and a much higher (during the second half of the release more than 200%) local Ca^{2+} level in cytosol, which both enhance the SERCA pump activity. In some cases this also resulted in greater net Ca^{2+} release during the spark, which in itself may increase wave-speed. Our model predicted that this effect is highly dependent on the CSQN distribution. If CSQN is distributed throughout Z-line SR, as suggested by electron microscopy studies, we predict that SERCA has a profound effect on both release duration and the net released Ca^{2+}. Release was prolonged as much as 20% and the net amount of Ca^{2+} was increased by as much as 10%.

The precise relationship between either of these SERCA-mediated changes and increased Ca^{2+} wave velocity is not straightforward to compute and is beyond the scope of this study. However, one thing that must be considered when proposing this hypothesis is that SERCA inhibition or activation may alter the threshold at which the spark terminates and thereby alter the potential for SERCA-mediated increase in net Ca^{2+} release. While such an effect was not observed as a result of thapsigargin blockade (Picht *et al.* 2011), the potential for enhanced SERCA activity to elicit alterations in the Fluo5 threshold has not been investigated.

NCX flux in the dyad does not alter the local Ca^{2+} concentration during a spark

In imunolabelling and electron tomography studies it has been disputed whether the NCX is included in the dyad or not (Trafford *et al.* 1995; Scriven *et al.* 2000; Jayasinghe *et al.* 2009). Both computational and experimental studies have also investigated whether NCX can contribute to EC coupling (Lines *et al.* 2006; Larbig *et al.* 2010). Here we used our model to predict the amount of Ca^{2+} that can be extruded from the CRU via NCX during a spark. Because the $[Ca^{2+}]$ in the dyad can be very high during a spark, we hypothesized that if NCX is included in the dyad, the amount of Ca^{2+} extracted from the cell should be substantial. Even though the $[Ca^{2+}]$ reached high concentrations, ~70 μM, the amount of Ca^{2+} extracted via NCX, when it was included in the dyad, did not alter the $[Ca^{2+}]$ markedly. This was primarily due to the small unitary current of NCX relative to the other dyadic fluxes. The current we predicted for a single NCX, 0.2 fA, is well below the theoretical maximum, 0.8 fA (Bers, 2001). However, even if we artificially increased the maximal current to 0.8 pA, the NCX were not able to alter the Ca^{2+} flux significantly. This suggests that the ability for NCX to alter $[Ca^{2+}]$ in the dyad during a spontaneously activated Ca^{2+} spark is limited, compared with other fluxes.

Software

Both electron tomography and light microscopy are generating new high-quality imaging data to describe subcellular structures (Scriven *et al.* 2000; Lukyanenko *et al.* 2007; Baddeley *et al.* 2009; Hayashi *et al.* 2009; Asghari *et al.* 2011). A challenge for data of this type is to convert these images into discretized geometries

that are suitable for use in computational models. For this study we have developed a pipeline that creates high-quality computational meshes from high-resolution image volumes. For the segmentation process we used well proven software, Imod (Kremer *et al.* 1996), to manually extract features of murine myocyte subcellular structure. Automated segmentation processes should ultimately improve the efficiency of this step (Pham *et al.* 2000; Volkmann, 2010; Helmstaedter & Mitra, 2012). We used our freely available software package GAMer (Yu *et al.* 2008b; www.fetk.org) to imropve the quality of the segmented mesh, and to further improve the usability of GAMer, we made it available as a plugin for the graphical user interface of Blender (www.blender.org), a feely available software tool for computer graphics and animation.

Limitations

Even though the present model includes a complete CRU, it was not large enough to harbour a full Ca^{2+} spark. For that a larger data set will be needed, particularly in the Z direction. We were therefore not able to generate a proper linescan from our generated geometry, but needed to do that from a separate and cruder model. To fit parameters to a proper linescan model is important as this is the only means to relate the model output to experimental Ca^{2+} spark measurements. A second limitation related to the small size of the geometry is that we needed to approximate the flux to the the cytosol using compartments external to the mesh, via the intermediate compartments, which have a homogeneous $[Ca^{2+}]$. This is an approximation, which will over- or underestimate the $[Ca^{2+}]$ outside the geometry, depending on the region in question, and this eventually causes the modelled outflux to be imprecise.

We have fitted our model to experimental measurements of SR $[Ca^{2+}]$ made in rabbit (Zima *et al.* 2008), but our geometry is constructed from electron tomograms of a mouse myocyte (Hayashi *et al.* 2009). As pointed out previously, it is inherently difficult to perform Fluo5 experiments in mouse and rats (Sobie & Lederer, 2012), and this limits the experimental assessments of Ca^{2+} movement during a spark for these species. That noted, features of Ca^{2+} movement inside the SR, and macroscopic features of SR Ca^{2+} release, such as fractional release, are similar in mouse and rabbit (Antoons *et al.* 2002).

Our model of the RyR termination is purely phenomenological, based on fitting of experimental Fluo5 measurements. A natural extension to the present study would be to introduce a better representation of the RyR model, for example one that is based on the model presented by Sobie *et al.* (2002). With such an extension we could investigate how well our model predicts how fractional release changes with SR Ca^{2+} content.

Conclusion

We have develop a detailed computational model of a cardiac Ca^{2+} spark based on a three dimensional reconstruction of electron tomography data. Our model predicts a severe Ca^{2+} depletion in junctional SR after a spark, while preserving a higher regional Ca^{2+} reserve, reconciling previous model predictions with experimental measurements. We also predict that a difference in local distribution of CSQN has a profound impact on spark termination time solely based on its Ca^{2+} buffering capacity. Finally we predict that local SERCA activity can prolong the spark by pumping Ca^{2+} back into junctional SR prior to termination of Ca^{2+} release.

References

Altamirano J & Bers DM (2007). Effect of intracellular Ca^{2+} and action potential duration on L-type Ca^{2+} channel inactivation and recovery from inactivation in rabbit cardiac myocytes. *Am J Physiol Heart Circ Physiol* **293**, H563–H573.

Antoons G, Mubagwa K, Nevelsteen I & Sipido KR (2002). Mechanisms underlying the frequency dependence of contraction and $[Ca^{2+}]_i$ transients in mouse ventricular myocytes. *J Physiol* **543**, 889–898.

Asghari P, Schulson M, Scriven DRL, Martens G & Moore EDW (2009). Axial tubules of rat ventricular myocytes form multiple junctions with the sarcoplasmic reticulum. *Biophys J* **96**, 4651–4660.

Asghari P, Scriven DRL, Hoskins J, Fameli N, van Breemen C & Moore EDW (2011). The structure and functioning of the couplon in the mammalian cardiomyocyte. *Protoplasma* **249**(Suppl 1), S31–38.

Baddeley D, Jayasinghe ID, Lam L, Rossberger S, Cannell MB & Soeller C (2009). Optical single-channel resolution imaging of the ryanodine receptor distribution in rat cardiac myocytes. *Proc Natl Acad Sci U S A* **106**, 22275–22280.

Bers DM (2001). *Excitation-Contraction Coupling and Cardiac Contractile Force*, 2nd edn. Kluwer Academic, Dordrecht, The Netherlands.

Bidwell P, Blackwell DJ, Hou Z, Zima AV & Robia SL (2011). Phospholamban binds with differential affinity to calcium pump conformers. *J Biol Chem* **286**, 35044–35050.

Bondarenko VE, Szigeti GP, Bett GCL, Kim SJ & Rasmusson RL (2004). Computer model of action potential of mouse ventricular myocytes. *Am J Physiol Heart Circ Physiol* **287**, H1378–1403.

Bossen EH, Sommer JR & Waugh RA (1981). Comparative stereology of mouse atria. *Tissue Cell* **13**, 71–77.

Cheng H, Lederer WJ & Cannell MB (1993). Calcium sparks: elementary events underlying excitation-contraction coupling in heart muscle. *Science* **262**, 740–744.

Cooper PJ, Soeller C & Cannell MB (2010). Excitation-contraction coupling in human heart failure examined by action potential clamp in rat cardiac myocytes. *J Mol Cell Cardiol* **49**, 911–917.

Dolber PC & Sommer JR (1984). Corbular sarcoplasmic reticulum of rabbit cardiac muscle. *J Ultrastruct Res* **87**, 190–196.

Fabiato A (1983). Calcium-induced release of calcium from the cardiac sarcoplasmic reticulum. *Am J Physiol Cell Physiol* **245**, C1–14.

Franzini-Armstrong C, Protasi F & Ramesh V (1999). Shape, size, and distribution of Ca^{2+} release units and couplons in skeletal and cardiac muscles. *Biophys J* **77**, 1528–1539.

Franzini-Armstrong C, Protasi F & Tijskens P (2005). The assembly of calcium release units in cardiac muscle. *Ann NY Acad Sci* **1047**, 76–85.

Gillespie D & Fill M (2008). Intracellular calcium release channels mediate their own countercurrent: the ryanodine receptor case study. *Biophys J* **95**, 3706–3714.

Györke I & Györke S (1998). Regulation of the cardiac ryanodine receptor channel by luminal Ca^{2+} involves luminal Ca^{2+} sensing sites. *Biophys J* **75**, 2801–2810.

Györke I, Hester N, Jones LR & Györke S (2004). The role of calsequestrin, triadin, and junctin in conferring cardiac ryanodine receptor responsiveness to luminal calcium. *Biophys J* **86**, 2121–2128.

Györke S, Stevens SCW & Terentyev D (2009). Cardiac calsequestrin: quest inside the SR. *J Physiol* **587**, 3091–3094.

Gómez AM, Cheng H, Lederer WJ & Bers DM (1996). Ca^{2+} diffusion and sarcoplasmic reticulum transport both contribute to $[Ca^{2+}]_i$ decline during Ca^{2+} sparks in rat ventricular myocytes. *J Physiol* **496**, 575–581.

Hayashi T, Martone ME, Yu Z, Thor A, Doi M, Holst MJ, Ellisman MH & Hoshijima M (2009). Three-dimensional electron microscopy reveals new details of membrane systems for Ca^{2+} signaling in the heart. *J Cell Sci* **122**, 1005–1013.

Helmstaedter M & Mitra PP (2012). Computational methods and challenges for large-scale circuit mapping. *Curr Opin Neurobiol* **22**, 162–169.

Hinch R, Greenstein JL, Tanskanen AJ, Xu L & Winslow RL (2004). A simplified local control model of calcium-induced calcium release in cardiac ventricular myocytes. *Biophys J* **87**, 3723–3736.

Jayasinghe ID, Cannell MB & Soeller C (2009). Organization of ryanodine receptors, transverse tubules, and sodium-calcium exchanger in rat myocytes. *Biophys J* **97**, 2664–2673.

Jorgensen AO, Shen AC, Arnold W, McPherson PS & Campbell KP (1993). The Ca^{2+}-release channel/ryanodine receptor is localized in junctional and corbular sarcoplasmic reticulum in cardiac muscle. *J Cell Biol* **120**, 969–980.

Jorgensen AO, Shen AC & Campbell KP (1985). Ultrastructural localization of calsequestrin in adult rat atrial and ventricular muscle cells. *J Cell Biol* **101**, 257–268.

Keller M, Kao JPY, Egger M & Niggli E (2007). Calcium waves driven by 'sensitization' wave-fronts. *Cardiovasc Res* **74**, 39–45.

Kettlun C, González A, Ríos E & Fill M (2003). Unitary Ca^{2+} current through mammalian cardiac and amphibian skeletal muscle ryanodine receptor channels under near-physiological ionic conditions. *J Gen Physiol* **122**, 407–417.

Kremer J, Mastronarde D & McIntosh J (1996). Computer visualization of three-dimensional image data using IMOD. *J Struct Biol* **116**, 71–76.

Lamont C, Luther PW, Balke CW & Wier WG (1998). Intercellular Ca^{2+} waves in rat heart muscle. *J Physiol* **512**, 669–676.

Larbig R, Torres N, Bridge JHB, Goldhaber JI & Philipson KD (2010). Activation of reverse Na^+-Ca^{2+} exchange by the Na^+ current augments the cardiac Ca^{2+} transient: evidence from NCX knockout mice. *J Physiol* **588**, 3267–3276.

Laver DR (2007). Ca^{2+} stores regulate ryanodine receptor Ca^{2+} release channels via luminal and cytosolic Ca^{2+} sites. *Biophys J* **92**, 3541–3555.

Lines GT, Sande JB, Louch WE, Mørk HK, Grøttum P & Sejersted OM (2006). Contribution of the Na^+/Ca^{2+} exchanger to rapid Ca^{2+} release in cardiomyocytes. *Biophys J* **91**, 779–792.

Logg A, Mardal KA, Wells GN (2012). *Automated Solution of Differential Equations by the Finite Element Method*. Springer, Berlin Heidelberg.

Louch WE, Hake J, Jølle GF, Mørk HK, Sjaastad I, Lines GT & Sejersted OM (2010). Control of Ca^{2+} release by action potential configuration in normal and failing murine cardiomyocytes. *Biophys J* **99**, 1377–1386.

Lukyanenko V, Ziman A, Lukyanenko A, Salnikov V & Lederer WJ (2007). Functional groups of ryanodine receptors in rat ventricular cells. *J Physiol* **583**, 251–269.

Maier LS, Zhang T, Chen L, DeSantiago J, Brown JH & Bers DM (2003). Transgenic CaMKIIdeltaC overexpression uniquely alters cardiac myocyte Ca^{2+} handling: reduced SR Ca^{2+} load and activated SR Ca^{2+} release. *Circ Res* **92**, 904–911.

Michailova A, DelPrincipe F, Egger M & Niggli E (2002). Spatiotemporal features of Ca^{2+} buffering and diffusion in atrial cardiac myocytes with inhibited sarcoplasmic reticulum. *Biophys J* **83**, 3134–3151.

Moraru II, Schaff JC, Slepchenko BM, Blinov ML, Morgan F, Lakshminarayana A, Gao F, Li Y & Loew LM (2008). Virtual cell modelling and simulation software environment. *IET Syst Biol* **2**, 352–362.

Page E (1978). Quantitative ultrastructural analysis in cardiac membrane physiology. *Am J Physiol Cell Physiol* **235**, C147–C158.

Pham DL, Xu C & Prince JL (2000). Current methods in medical image segmentation. *Annu Rev Biomed Eng* **2**, 315–337.

Picht E, Zima AV, Shannon TR, Duncan AM, Blatter LA & Bers DM (2011). Dynamic calcium movement inside cardiac sarcoplasmic reticulum during release. *Circ Res* **108**, 847–856.

Ramay HR, Jafri MS, Lederer WJ & Sobie EA (2010). Predicting local SR Ca^{2+} dynamics during Ca^{2+} wave propagation in ventricular myocytes. *Biophys J* **98**, 2515–2523.

Ramay HR, Liu OZ & Sobie EA (2011). Recovery of cardiac calcium release is controlled by sarcoplasmic reticulum refilling and ryanodine receptor sensitivity. *Cardiovasc Res* **91**, 598–605.

Restrepo JG, Weiss JN & Karma A (2008). Calsequestrin-mediated mechanism for cellular calcium transient alternans. *Biophys J* **95**, 3767–3789.

Rice JJ, Jafri MS & Winslow RL (1999). Modeling gain and gradedness of Ca^{2+} release in the functional unit of the cardiac diadic space. *Biophys J* **77**, 1871–1884.

Robertson SP, Johnson JD & Potter JD (1981). The time-course of Ca^{2+} exchange with calmodulin, troponin, parvalbumin, and myosin in response to transient increases in Ca^{2+}. *Biophys J* **34**, 559–569.

Scriven DR, Dan P & Moore ED (2000). Distribution of proteins implicated in excitation-contraction coupling in rat ventricular myocytes. *Biophys J* **79**, 2682–2691.

Shannon TR & Bers DM (1997). Assessment of intra-SR free [Ca] and buffering in rat heart. *Biophys J* **73**, 1524–1531.

Shannon TR, Ginsburg KS & Bers DM (2000*a*). Potentiation of fractional sarcoplasmic reticulum calcium release by total and free intra-sarcoplasmic reticulum calcium concentration. *Biophys J* **78**, 334–343.

Shannon TR, Ginsburg KS & Bers DM (2000*b*). Reverse mode of the sarcoplasmic reticulum calcium pump and load-dependent cytosolic calcium decline in voltage-clamped cardiac ventricular myocytes. *Biophys J* **78**, 322–333.

Shannon TR, Guo T & Bers DM (2003). Ca^{2+} scraps: local depletions of free $[Ca^{2+}]$ in cardiac sarcoplasmic reticulum during contractions leave substantial Ca^{2+} reserve. *Circ Res* **93**, 40–45.

Smith GD, Keizer JE, Stern MD, Lederer WJ & Cheng H (1998). A simple numerical model of calcium spark formation and detection in cardiac myocytes. *Biophys J* **75**, 15–32.

Sobie EA, Dilly KW, dos Santos Cruz J, Lederer WJ & Jafri MS (2002). Termination of cardiac Ca^{2+} sparks: an investigative mathematical model of calcium-induced calcium release. *Biophys J* **83**, 59–78.

Sobie EA & Lederer WJ (2012). Dynamic local changes in sarcoplasmic reticulum calcium: Physiological and pathophysiological roles. *J Mol Cell Cardiol* **52**, 304–311.

Song LS, Sobie EA, McCulle S, Lederer WJ, Balke CW & Cheng H (2006). Orphaned ryanodine receptors in the failing heart. *Proc Natl Acad Sci U S A* **103**, 4305–4310.

Stern MD (1992). Theory of excitation-contraction coupling in cardiac muscle. *Biophys J* **63**, 497–517.

Swietach P, Spitzer KW & Vaughan-Jones RD (2010). Modeling calcium waves in cardiac myocytes: importance of calcium diffusion. *Front Biosci* **15**, 661–680.

Ter Keurs HEDJ & Boyden PA (2007). Calcium and arrhythmogenesis. *Physiol Rev* **87**, 457–506.

Toyoshima C (2008). Structural aspects of ion pumping by Ca^{2+}-ATPase of sarcoplasmic reticulum. *Arch Biochem Biophys* **476**, 3–11.

Trafford AW, Díaz ME, O'Neill SC & Eisner DA (1995). Comparison of subsarcolemmal and bulk calcium concentration during spontaneous calcium release in rat ventricular myocytes. *J Physiol* **488**, 577–586.

Tran K, Smith NP, Loiselle DS & Crampin EJ (2009). A thermodynamic model of the cardiac sarcoplasmic/endoplasmic Ca^{2+} (SERCA) pump. *Biophys J* **96**, 2029–2042.

Valent I, Zahradníková A, Pavelková J & Zahradník I (2007). Spatial and temporal Ca^{2+}, Mg^{2+}, and ATP^{2-} dynamics in cardiac dyads during calcium release. *Biochim Biophys Acta* **1768**, 155–166.

Volkmann N (2010). Methods for segmentation and interpretation of electron tomographic reconstructions. *Methods Enzymol* **483**, 31–46.

Wang SQ, Stern MD, Ríos E & Cheng H (2004). The quantal nature of Ca^{2+} sparks and in situ operation of the ryanodine receptor array in cardiac cells. *Proc Natl Acad Sci U S A* **101**, 3979–3984.

Williams G, Chikando A, Tuan HTM, Sobie E, Lederer W & Jafri M (2011). Dynamics of calcium sparks and calcium leak in the heart. *Biophys J* **101**, 1287–1296.

Yu Z, Holst MJ, Hayashi T, Bajaj CL, Ellisman MH, McCammon JA & Hoshijima M (2008*a*). Three-dimensional geometric modeling of membrane-bound organelles in ventricular myocytes: Bridging the gap between microscopic imaging and mathematical simulation. *J Struct Biol* **164**, 304–313.

Yu Z, Holst MJ & McCammon JA (2008*b*). High-fidelity geometric modeling for biomedical applications. *Finite Elem Anal Des* **44**, 715–723.

Zima AV, Picht E, Bers DM & Blatter LA (2008). Termination of cardiac Ca^{2+} sparks: role of intra-SR $[Ca^{2+}]$, release flux, and intra-SR Ca^{2+} diffusion. *Circ Res* **103**, e105–e115.

Author contributions

J.H. was the main author of the manuscript and the revised version, and significantly contributed to the design, analysis and interpretation of the computational experiments. A.G.E. significantly contributed to the design, analysis and interpretation of the computational experiments, and also significantly contributed to the drafting and revision of the manuscript. Z.Y. significantly contributed to the design of the computational experiments and significantly contributed in the drafting and revision of the manuscript. P.M.K.-H. significantly contributed to the design and interpretation of the computational experiments and significantly contributed in the drafting and revision of the manuscript. A.P.M. significantly contributed to the design and interpretation of the computational experiments and significantly contributed in the drafting of the manuscript. J.A.M. significantly contributed to the interpretation of the computational experiments and significantly contributed in the drafting of the manuscript. M.J.H. significantly contributed to the design of the computational experiments and significantly contributed in the drafting of the manuscript. M.H. significantly contributed to the design and interpretation of the computational experiments and significantly contributed in the drafting and revision of the manuscript. A.D.M. significantly contributed to the design and interpretation of the computational experiments and significantly contributed in the drafting and revision of

the manuscript. All authors approved the final version for publication.

Acknowledgements

This work was supported by the National Biomedical Computational Resource NIH grant 8P41GM103426-19 and NIH grant 1R01 HL96544. The work was also partially supported from the Center for Theoretical Biological Physics (NSF PHY-0822283), NIH grant 1R01 GM31749, NIH grant 5P01HL46345, NIH grant RR004050/GM103412, Centre of Excellence grant from the Research Council of Norway to the Centre for Biomedical Computing at Simula Research Laboratory, AGE was a Fellow of the Heart Rhythm Society, and by American Heart Association Established Investigator Award 0840013N. We thank William E. Louch for helpful suggestions during the study and Jerry Tsai for his dedicated help during the development of the model.